

Synthesis of Polymer Coated Iron Oxide Nanoparticles for Drug Release by Applying Alternating Magnetic Field



By

Reema Ansar

(Registration No: 00000363809)

Department of Chemical Engineering

School of Chemical and Materials Engineering

National University of Sciences & Technology (NUST)

Islamabad, Pakistan

(2024)

Synthesis of Polymer Coated Iron Oxide Nanoparticles for Drug Release by Applying Alternating Magnetic Field



By

Reema Ansar

(Registration No: 00000363809)

A thesis submitted to the National University of Sciences and Technology, Islamabad,

in partial fulfillment of the requirements for the degree of

Master of Science in
Chemical Engineering

Supervisor: Dr. Zaib Jahan

Co Supervisor: Dr. Usman Liaqat

School of Chemical and Materials Engineering

National University of Sciences & Technology (NUST)

Islamabad, Pakistan

(2024)



THESIS ACCEPTANCE CERTIFICATE

Certified that final copy of MS thesis written by Ms **Reema Ansar** (Registration No 00000363809), of School of Chemical & Materials Engineering (SCME) has been vetted by undersigned, found complete in all respects as per NUST Statues/Regulations, is free of plagiarism, errors, and mistakes and is accepted as partial fulfillment for award of MS degree. It is further certified that necessary amendments as pointed out by GEC members of the scholar have also been incorporated in the said thesis.

Signature: *Dr Zaib Jahan*

Name of Supervisor: Dr Zaib Jahan

Date: _____

Signature (HOD): *[Signature]*

Date: 02/10/2024

Signature (Dean/Principal): *[Signature]*

Date: 3/10/24



National University of Sciences & Technology (NUST)

MASTER'S THESIS WORK

Formulation of Guidance and Examination Committee (GEC)

Name: Reema Ansar
Department: Department of Chemical Engineering

NUST Reg No: 00000363809
Specialization: Master of Science in Chemical Engineering
CGPA: 3.83

Credit Hour Completed: 18.0

Course Work Completed

S/No:	Code:	Title:	Core/Elective:	CH:	Grade:
1.	HE-815	Nano Catalysis	Elective	3.0	B+
2.	CHE-843	Separation Processes In Che	Compulsory	3.0	A
3.	CHE-847	Chemical Kinetics & Reactor Design	Compulsory	3.0	A
4.	RM-898	Research Methodology	Additional	2.0	Q
5.	EME-921	Momentum, Heat & Mass Transfer In Chemical Engineering Separation Processes	Compulsory	3.0	B+
6.	CHE-14	Product Technology	Elective	3.0	A
7.	ENS-830	Cleaner Production Technologies	Elective	3.0	A

Date: 02 - Nov - 2022

Thesis Committee

Name: Zaib Jahan (Supervisor)
Department: Department of Chemical Engineering

Name: Usman Liaqat (Cosupervisor)
Department: Department of Materials Engineering

Name: Muhammad Bilal Khan Niazi (Internal)
Department: Department of Chemical Engineering

Name: Iftikhar Hussain Gul (Internal)
Department: Department of Materials Engineering

Name: Zaib Jahan (External)
Department: Department of Chemical Engineering

Student's Signature

Signature

Signature

Signature

Signature

Signature

Signature of Head of Department:

Date: 02 - Nov - 2022

APPROVAL



National University of Sciences & Technology (NUST)

FORM TH-4

MASTER'S THESIS WORK

We hereby recommend that the dissertation prepared under our supervision by

Regn No & Name: 00000363809 Reema Ansar

Title: Synthesis of Polymer Coated Iron Oxide Nanoparticles for Drug Release by Applying Alternating Magnetic Field.

Presented on: 21 Aug 2024 at: 1500 hrs in SCME Seminar Hall

Be accepted in partial fulfillment of the requirements for the award of Master of Science degree in Chemical Engineering.

Guidance & Examination Committee Members

Name: Dr Sulalit Bandyopadhyay (NTNU)

Signature: Sulalit Bandyopadhyay

Name: Dr Iftikhar Hussain Gul

Signature: Iftikhar Hussain Gul

Name: Dr M. Bilal Khan Niazi

Signature: M. Bilal Khan Niazi

Name: Dr Usman Liaqat (Co-Supervisor)

Signature: Usman Liaqat

Supervisor's Name: Dr Zaib Jahan

Signature: Zaib Jahan

Dated: 26-8-2024

[Signature]
Head of Department

Date 29-08-2024

[Signature]
Dean/Principal

Date 29/8/24

School of Chemical & Materials Engineering (SCME)

AUTHOR'S DECLARATION

IReema Ansar..... hereby state that my MS thesis titled “**Synthesis of Polymer Coated Iron Oxide Nanoparticles for Drug Release by Applying Alternating Magnetic Field**” is my own work and has not been submitted previously by me for taking any degree from National University of Sciences and Technology, Islamabad or anywhere else in the country/world.

At any time if my statement is found to be incorrect even after I graduate, the university has the right to withdraw my MS degree.

Name of Student: Reema Ansar

Date: 05.12.2024

DEDICATION

By the grace of Almighty Allah, who is the most beneficent and the most merciful.

This thesis is dedicated to my parents and siblings who trusted me and supported me in my every decision.

To my supervisors who guided me and shared their knowledge. Who encouraged me throughout this journey.

ACKNOWLEDGEMENT

I would like to thank my supervisor **Dr. Zaib Jahan** and express my heartfelt gratitude for your unwavering support and guidance throughout my research. I would also like to extend my sincere appreciation to **Dr. Muhammad Bilal Khan Niazi** for his support, especially through building up a research base. I am deeply thankful for their patience, dedication, and commitment to my academic and professional development. Their support led me to grab the prestige Erasmus Exchange position at Norwegian University of Science and Technology (NTNU) making the way to work with a well-organized and a smart research team. I would like to thank my Co-Supervisor at NUST **Dr. Usman Liaqat** and GEC member **Dr. Iftikhar Hussain Gul** for their guidance.

I want to thank my supervisor at NTNU, **Dr. Sulalit Bandyopadhyay** for his experimental suggestions, and valuable feedback. Your expertise and guidance were invaluable in helping me overcome the challenges that I encountered during the project. Your insightful comments, constructive criticism, and valuable suggestions have been instrumental in shaping the success of my project. I learned a lot and developed my interpersonal and research skills. Moreover, I would like to thank **Nesrine Bali** for sharing the knowledge and experimental skills throughout my research. From teaching me to hold the pipette in the right way to designing the experiments, you have been a true guide in my initial research phase in the lab. Thanks for teaching me the holistic approach in research. Then I pay my regards to the particle engineering research team for their support, especially the engineers, Hammad and Tobias. Thank you for helping me in learning new characterization techniques. Then, I would like to thank my colleagues (Hizbullah and Sarmad) for their useful input and making a very healthy learning environment. Also, the contact angle measurements were done by Hizbullah Malik. Thanks to the engineers working at NUST for their help in completing my research studies. I owe my limitless thanks to my parents and siblings. Their unconditional love, trust and support were my energy pill which kept me going throughout this journey.

TABLE OF CONTENTS

TABLE OF CONTENTS	ix
LIST OF TABLES	xi
LIST OF FIGURES	xii
LIST OF SYMBOLS, ABBREVIATIONS and acronyms	xiv
ABSTRACT	xv
CHAPTER 1: INTRODUCTION	1
CHAPTER 2 : THEORY	3
2.1 Nanoparticles	3
2.1.1 <i>Crystallization and Classical Nucleation Theory</i>	3
2.1.2 <i>Iron Oxide Nanoparticles</i>	7
2.1.3 <i>Methods for Polymer coating of IONPs</i>	14
2.1.4 <i>Polymer coated Iron oxide nanoparticles for theranostics</i>	20
CHAPTER 3: MATERIALS AND METHODS	25
3.1 Materials	25
3.2 Synthesis of Oleic acid coated Iron Oxide Nanoparticles	25
3.2.1 <i>Method I</i>	25
3.2.2 <i>Method II</i>	26
3.3 Optimization with different amounts of Oleic acid	27
3.4 Synthesis of PLGA nanoparticles	27
3.5 Synthesis of PLGA coated Iron Oxide nanoparticles	27
3.6 Optimization with different PLGA and IONPs concentrations	28
3.7 Methods for the characterization	28
3.7.1 <i>Fourier-Transform Infrared-Attenuated Total Reflection (FTIR)</i>	28
3.7.2 <i>Thermogravimetric analysis (TGA)</i> :.....	29
3.7.3 <i>Dynamic Light Scattering (DLS)</i> :.....	30
3.7.4 <i>Scanning Transmission Electron Microscope S(T)EM</i>	30
3.7.5 <i>Vibrating sample magnetometer (VSM)</i>	32
3.7.6 <i>Drop Shape Analyzer (DSA)</i>	32
3.7.7 <i>X-Ray Crystallography (XRD)</i>	33
3.7.8 <i>Magnetherm</i>	34
3.7.9 <i>Software</i>	35

CHAPTER 4: RESULTS AND DISCUSSIONS.....	36
4.1 Synthesis of Iron oxide nanoparticles.....	36
4.1.1 <i>Method I</i>	36
4.1.2 <i>Method II</i>	38
4.2 Synthesis of bare PLGA nanoparticles.....	44
4.2.1 <i>STEM images and hydrodynamic dia of bare PLGA nanoparticles</i>	44
4.2.2 <i>Optimization with different PLGA weight %</i>	45
4.3 Synthesis of PLGA coated Iron Oxide nanoparticles.....	46
4.3.1 <i>S(T)EM images and Hydrodynamic dia of PNPs@IONPs</i>	46
4.3.2 <i>Energy Dispersive Spectroscopy (EDS) of particles</i>	47
4.3.3 <i>Optimization with different IONPs concentrations</i>	48
4.3.4 <i>FTIR of OA-IONPs, PNPS and PNPs@IONPs</i>	48
4.3.5 <i>TGA of OA-IONPs, PNPS and PNPs@IONPs</i>	49
4.3.6 <i>VSM of PNPs@IONPs</i>	50
4.4 Hyperthermia and Drug release.....	51
4.4.1 <i>Hyperthermia and SAR Values</i>	51
4.4.2 <i>Drug release</i>	53
SUMMARY OF RESEARCH WORK.....	59
CHAPTER 5: CONCLUSION AND FUTURE RECOMMENDATIONS.....	60
REFERENCES.....	61

LIST OF TABLES

	Page No
Table 2.1 Summary of various methods of IONPs synthesis.....	10
Table 2.2: Advantages of organic and inorganic coatings on IONPs	12
Table 2.3: Methods for coating/encapsulation of IONPs by polymer.....	14
Table 2.4 Summary based on literature survey for Polymer coated Iron oxide nanoparticles for cancer treatment	22

LIST OF FIGURES

	Page No
Figure 2-1 Conceptual picture of the mechanism of nucleation according to classical nucleation theory.....	5
Figure 2-2 The relationship between the precipitate radius and the free energy of homogeneous and heterogeneous nucleation.	6
Figure 2-3 La Mer Diagram: formation of NPs through Supersaturation	7
Figure 2-4 Ferromagnetism behavior of materials	9
Figure 2-5 The application of an external magnetic field that causes superparamagnetic particles to become magnetized. Saturation magnetization is known as M_s	10
Figure 2-6 Structural formula of oleic acid.....	14
Figure 2-7 Flash nanoprecipitation setup and common reactor types (confined impingement jet (CIJ) and multi inlet vortex mixer (MIVM)).....	16
Figure 2-8 La Mer Diagram: formation of NPs through Supersaturation (S) in FNP reactor.....	18
Figure 3-1: Synthesis of oleic acid coated Iron oxide nanoparticles.....	26
Figure 3-2: Synthesis of oleic acid coated Iron oxide nanoparticles.....	26
Figure 3-3:Flash nanoprecipitation setup.....	27
Figure 3-4(a)Bruker Vertex 80v FTIR Spectrometer (b) Schematic showing the main components of FTIR.....	29
Figure 3-5(a) Netzsch TG209F1 TGA (b) Schematic of components of TGA.....	29
Figure 3-6: Anton Paar LiteSizer 500.....	30
Figure 3-7 (a)High resolution S(T)EM Components (b) Schematic showing the main components of S(T)EM	31
Figure 3-8: Vibrating sample magnetometer (VSM)	32
Figure 4-1: XRD pattern of IONPs	36
Figure 4-2 S(T)EM images of IONPs	37
Figure 4-3 VSM of IONPs	38
Figure 4-4 XRD of bare and oleic acid coated IONPs.....	39
Figure 4-5 S(T)EM of bare and oleic acid coated IONPs.....	40
Figure 4-6 Hydrodynamic dia of(a)bare and (b) oleic acid coated IONPs	40
Figure 4-7 VSM of bare and oleic acid coated IONPs.....	41
Figure 4-8 FTIR of oleic acid, bare IONPs and oleic acid coated IONPs	42
Figure 4-9 Contact angle of (a) bare IONPs and (b) oleic acid coated IONPs	43
Figure 4-10 Optimization of particle size with increasing oleic acid volumes	44
Figure 4-11 S(T)EM images of bare polymeric particles.....	45
Figure 4-12 Hydrodynamic dia of bare polymeric particles	45
Figure 4-13 Optimization of particle size with increasing PLGA wt%	46
Figure 4-14 S(T)EM images of Polymer encapsulated IONPs.....	47
Figure 4-15 Hydrodynamic dia of Polymer encapsulated IONPs.....	47
Figure 4-16 EDS of Polymer encapsulated IONPs	47
Figure 4-17 S(T)EM images for increasing concentration of IONPs in polymer encapsulated IONPs.....	48
Figure 4-18 FTIR of OA-IONPs, PNPs and PNPs@IONPs	49

Figure 4-19: TGA of IONPs,OA-IONPs, PNPS and PNP@IONPs	50
Figure 4-20 VSM of IONPs , OA-IONPs and PNP@IONPs	50
Figure 4-21 (a) Optimization for maximum SAR value at 1mg/ml at Brozovich limit (b) Optimization for maximum SAR value at 1mg/ml at 5X Brezovich limit	52
Figure 4-22 SAR values at different concentrations of IONPs.....	52
Figure 4-23: SAR values of bare IONPs and PNP@IONPs.....	53
Figure 4-24 Absorbance peaks for Paclitaxel at different concentrations(mg/ml).....	54
Figure 4-25 Paclitaxel UV-Vis calibration curve with the Lambert-Beer law.....	54
Figure 4-26 (a) drug release in absence of magnetic field (b) drug release in applied magnetic field	55
Figure 4-27: Controlled drug release in pulsed magnetic field, textured area represents when the magnetic field is turned on.....	56
Figure 4-28 Controlled drug release in pulsed magnetic field, textured area represents when the magnetic field is turned on.....	56
Figure 4-29: Controlled drug release in pulsed magnetic field, textured area represents when the magnetic field is turned on.....	57
Figure 4-30: Controlled drug release in pulsed magnetic field, textured area represents when the magnetic field is turned on.....	58

LIST OF SYMBOLS, ABBREVIATIONS AND ACRONYMS

CIJ	Confined Impinging Jet
CNT	Classical Nucleation Theory
EDX	Energy Dispersive X-ray Spectroscopy
FNP	Flash Nanoprecipitation
FTIR	Fourier-Transform Infrared-Attenuated Total Reflection
MIVM	Multi-inlet vortex mixer
IONPS	Iron Oxide Nanoparticles
OA-IONPS	Oleic Acid coated Iron Oxide Nanoparticles
PLGA	Poly(lactide-co-glycolic acid)
PTX	Paclitaxel
PNPs	Polymeric Nanoparticles
PNPS @IONPs	Polymer encapsulated Iron Oxide Nanoparticles
PEG	Polyethylene glycol
PVA	Polyvinyl Alcohol
PMMA	Polymethyl methacrylate
PLA	Polylactic acid
S(T)EM	Scanning Transmission Electron Microscopy
XRD	X-Ray Crystallography

ABSTRACT

Magnetically controlled drug release is a promising alternative to conventional cancer treatment, having the potential to improve the therapeutic effect and decrease side effects. Iron oxide nanoparticles (IONPs) offer promising potential for magnetically controlled drug release due to their superparamagnetic properties and tunable surface characteristics. By incorporating drugs into or onto these nanoparticles and coating them with biocompatible polymers, such systems can be created where drug release is triggered or modulated by external magnetic fields.

In this study IONPs were synthesized by co-precipitation method and functionalized with oleic acid to incorporate hydrophobicity to them. An optimization study for the effect of amount of oleic acid was conducted. For 1.2ml of oleic per 200mg of IONPs the hydrodynamic size of IONPs was observed to be minimum i.e., $57\text{nm}\pm 0.27$. These optimized IONPs were encapsulated in poly(lactic-co-glycolic acid), PLGA using Flash Nanoprecipitation. Flash nanoprecipitation is a versatile and scalable technique used for the rapid and efficient encapsulation of hydrophobic drugs or other compounds into nanoparticles. Initially, bare PLGA nanoparticles were made by flash nanoprecipitation, after optimizing the conditions for bare PLGA nanoparticles, Paclitaxel and IONPs were co-encapsulated in PLGA. The encapsulation was confirmed with different characterization techniques such as STEM,EDX, FTIR and magneTherm. It was observed as the concentration of IONPs in flash nanoprecipitation is increased from 1mg/ml to 3mg/ml more encapsulated in PLGA. But for concentration 4mg/ml to 6mg/ml the IONPs precipitate faster than PLGA and attach to the outside surface of PLGA instead of being encapsulated. Magnetically controlled drug release was studied using the magneTherm. The results indicated that it is possible to co-encapsulate Paclitaxel and IONPs in PLGA using flash nanoprecipitation. And we can observe magnetically controlled drug release from these encapsulated nanoparticles.

CHAPTER 1: INTRODUCTION

Nanotechnology has emerged as a promising means for investigating new approaches to detect and treat complex diseases. Various nanoparticle-based drug delivery systems are being designed to achieve specific advantages e.g., greater stability, biocompatibility, increased permeability, retention effect and precision targeting over conventional drug delivery. Combining two materials, encapsulating iron oxide nanoparticles in polymeric nanoparticles can result in potential hybrid nanoparticles for biomedical applications. Iron oxide nanoparticles (IONPs) can be utilized to produce hyperthermia, deliver medicines to specific tissues, and/or serve as a contrast agent. The polymer shell works as a transport agent, reducing the toxicity of the iron core, increasing bioavailability, and allowing for longer *in vivo* stability. The shell can be changed to block certain interactions while allowing other processes and interactions with cells to take place. Highly optimized hybrid metal-polymer systems can be designed to treat diseases such as cancer.

Nanocarriers (NCs) can be used to deliver active therapeutic substances in a controlled manner, which can lead to a number of benefits, including increased overall efficacy, sustained activity, less toxicity, easier dosage regimens, and better patient adherence.[1]. The desire to use the nanoparticle to target delivery and subsequently release cargo at the desired target site is a primary drive for NC formulations. Direct precipitation methods are appealing because they produce NCs with high mass loadings in a scalable and continuous manner, as in the case of Flash Nanoprecipitation (FNP)[2-4]. Hydrophobic active pharmaceutical ingredients (APIs) are commonly dissolved in organic solvents and combined with water as an antisolvent in flash nanoprecipitation techniques to induce precipitation. Recent research studies are focusing on dual drug delivery systems. One example of such systems is magnetic nanoparticles that can induce magnetic hyperthermia as well as serve as nanocarriers for drug.

Magnetic hyperthermia is a promising cancer treatment approach that uses magnetic nanoparticles to generate heat within tumors. This heat is produced by applying an alternating magnetic field to the nanoparticles, which causes them to oscillate and produce heat through hysteresis losses. The elevated temperatures induced by magnetic hyperthermia can selectively destroy cancer cells while

sparing healthy tissue. Treatment for cancer is one of the many biomedical uses for the magnetic hyperthermia effect. Temperature fluctuation, on the other hand, can be used to facilitate regulated release of drugs by promoting structural modification in nanostructured multifunctional systems (nanocarriers). Paclitaxel (PTX), a medicine produced from the bark of *Taxus brevifolia*, has attracted attention for its efficacy against numerous types of cancer, including ovarian, breast, lung, and prostate cancer. However, PTX has a low water solubility and is harmful to normal cells due to its low selective and non-specific body distribution. Drug delivery techniques such liposomes, solid lipid nanoparticles, polymeric nanoparticles, and micellar systems for the controlled release of paclitaxel into the tumor environment have been researched as a way to get around these restrictions.

[5].

In the present study, PTX and IONPs are co-encapsulated in PLGA and evaluated in regard to its potential as a magnetic-responsive drug delivery system. Physicochemical characterization, magnetic property analysis, and *in vitro* drug release experiments were carried out to help achieve this goal.

CHAPTER 2 : THEORY

The theoretical groundwork required to comprehend the work done in this research thesis is covered in this chapter. This includes the theories of nanoparticle nucleation and growth, the magnetic properties of iron oxide nanoparticles, and the stimuli responsive polymers and drug release. Previous research in these areas for the use of targeted drug delivery is also covered in this chapter.

2.1 Nanoparticles

Nanoparticles are colloidal particles with sizes between 10 and 1000 nm with at least one dimension less than 100 nm [6]. Compared to bigger particles, nanoparticles have various advantages, such as a higher surface-to-volume ratio. The use of nanoparticles in many biomedical applications, including targeted delivery of drugs, hyperthermia, photoablation treatment, bioimaging, and biosensors, has been gaining popularity during the past few years [6].

Before discussing the different types and applications of nanoparticles, it is important to discuss the classical nucleation and growth theory as its crucial for understanding of nanoparticle formation.

2.1.1 Crystallization and Classical Nucleation Theory

The most popular theoretical model for studying the dynamics of nucleation quantitatively is classical nucleation theory (CNT). After nucleation comes crystal growth. Controlling the crystallization process enables tuning of properties such as composition, shape, size, polydispersity, and crystallinity. For instance, crystallinity, which refers to the degree of atoms' long-range ordering in the lattice, has a significant impact on magnetic characteristics[7]. To control these properties, understanding of the process is essential, especially when the application is in biomedical field[8]. The crystallization process will be discussed now with an emphasis on magnetic nanoparticles for biomedical uses[9].

The first step to the formation of NPs in solution is nucleation. To describe nucleation, one must first define the driving force for crystallization. It can be defined as the difference between a

solute molecule's chemical potential in the solution's equilibrium state, μ_2 , and its current state, μ_1 . It is more practical to express this driving force in terms of the supersaturation S in practical applications.

$$\Delta\mu = \mu_1 - \mu_2 = kT \ln S = kT \ln \left(\frac{a}{a^*} \right) = kT \ln (s) \quad (2.1)$$

where μ_1 and μ_2 are the chemical potentials of the solute in the solution and in the solid phase, respectively, the variables k , T , and a denote the concentration and equilibrium state of the solution, supersaturated solution activity (a) and solution equilibrium activity (a^*), respectively (notice that $a = c\gamma$, where c is the concentration and γ its activity coefficient). Even though the final step in Eq. (2.1), which substitutes concentrations for activities, is only accurate in ideal solutions, where $\gamma \approx \gamma^* \approx 1$ or when $\gamma/\gamma^* \approx 1$ (a far less strict requirement), it still serves as a useful approximation because concentrations are quantities that can be measured experimentally. [9].

According to classical nucleation theory, simultaneous changes in density and order lead to the formation of crystalline clusters from the supersaturated solution. Step-by-step attachments and detachments of the solute molecules that serve as the building blocks of crystals are possible. The blue pathway shown in Figure 2.1 travels reversibly when molecules are attaching or detaching, depending on the rates of molecular attachment and detachment. The attachment of molecules to a cluster is energetically unfavorable up to a certain number of molecules, after which it is favored.

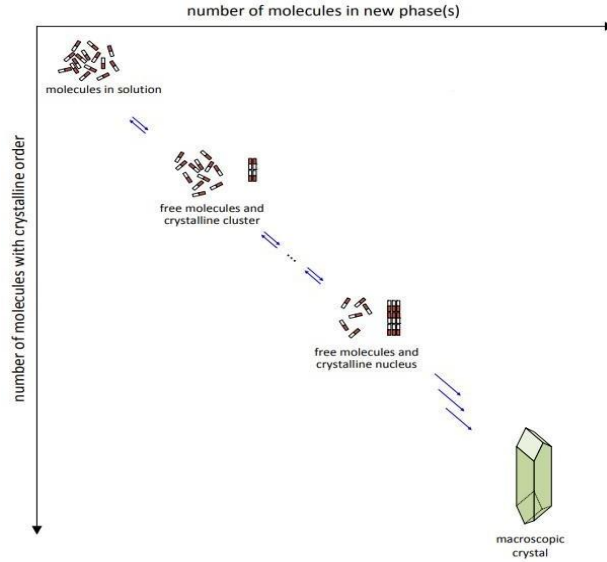


Figure 2-1 Conceptual picture of the mechanism of nucleation according to classical nucleation theory [10]

An equation in the Arrhenius form can be used to express the nucleation rate of N nuclei generated per unit time per unit volume

$$J = \frac{dN}{dt} = A \exp\left(\frac{\Delta G_{crit}}{K_B T}\right) \quad (2.2)$$

where ΔG_{crit} is the minimum energy barrier required to get stable nuclei in solution. A is a pre-exponential factor. For homogenous nucleation of spherical particles,

$$\Delta G_{crit} = \frac{16\pi\gamma^3 v^2}{3(k_B T \ln S)^2} \quad (2.3)$$

where γ is the interfacial tension, v is the molecular volume. This results in the final nucleation rate expression, which indicates that the rate is controlled by temperature, supersaturation, and interfacial tension.

$$J = A \exp\left[-\frac{16\pi\gamma^3 v^2}{3(k_B T \ln S)^2}\right] \quad (2.4)$$

Homogeneous and heterogeneous nucleation are two different types of nucleation. The process of monomeric units converging in a supersaturated fluid has just been described as homogeneous nucleation. On the other side, heterogeneous nucleation lowers the energy barrier of nucleation by introducing a surface to the media, as illustrated in Figure 2.2. $\Delta G^*_{het} = \phi \Delta G^*_{hom}$, is the expression that represents the relationship between the free energies, where ϕ is a factor that ranges from zero to one and is dependent on the contact angle between the particle and the solution[9, 10].

As heterogeneous nucleation requires less surface area to generate nuclei and has lower interfacial energy than liquid-solid phases, it has a lower critical energy. The term "heterogeneous nucleation" describes the nucleation at the surface of foreign objects, such as suspended particles, contaminants, and the surfaces of heat exchangers and containers.

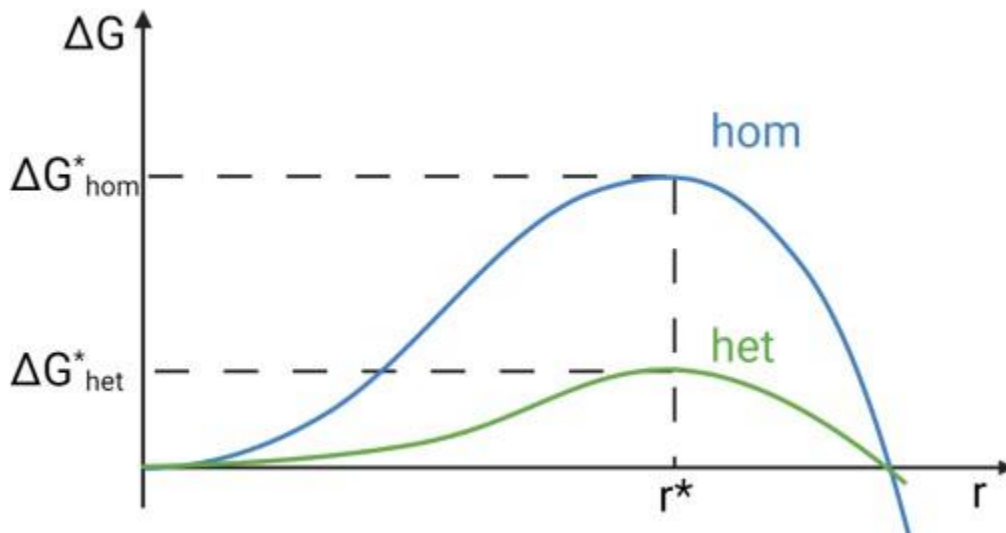


Figure 2-2 The relationship between the precipitate radius and the free energy of homogeneous and heterogeneous nucleation.

While the critical energy is noticeably higher for homogeneous nucleation, the critical radius is the same. The illustration is based on work by Bandyopadhyay[10].

The ultimate particle size is determined by the relative rates of nucleation and growth, since these processes compete for the consumption of monomeric units. Because more monomeric units will be consumed in the process of creating new nuclei, a high nucleation rate will produce many tiny particles. Conversely, a higher growth rate will cause larger particles by causing existing particles to consume more monomeric units. One significant element affecting these relative rates is supersaturation. At low supersaturation, between c_{\min} and c_s , only growth is possible; at high supersaturation, a significant nucleation rate will occur as shown in Fig 2.3. Particle size can also be influenced by kinetic parameters through spatial confinement, such as capping agents.

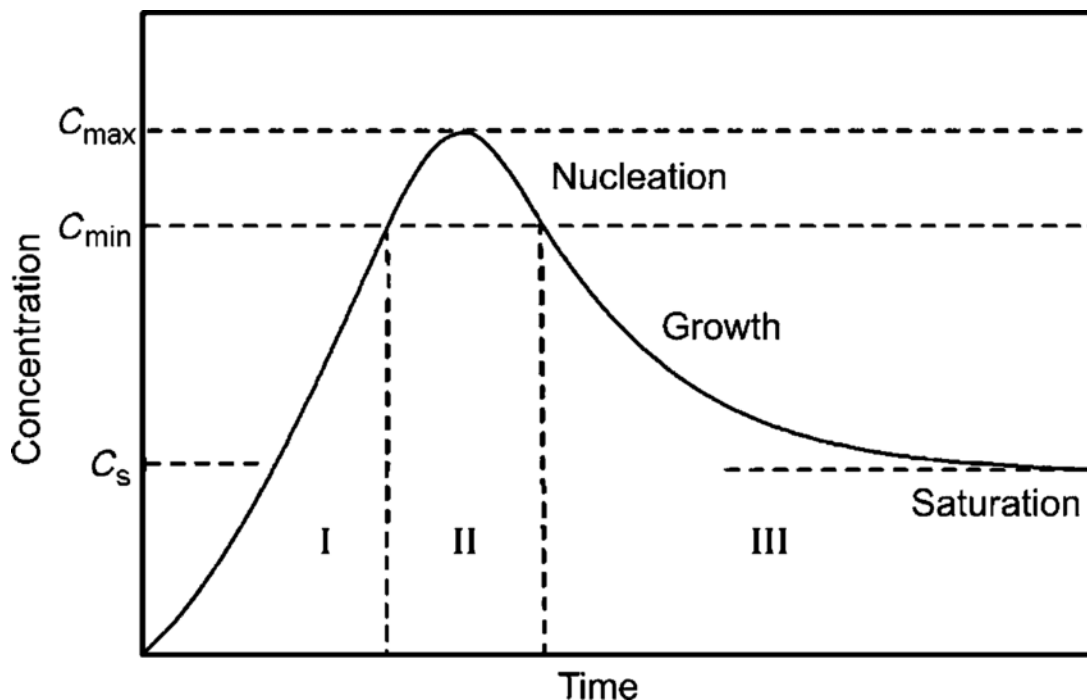


Figure 2-3 La Mer Diagram: formation of NPs through Supersaturation[11]

Particles with identical qualities are produced via a controlled size distribution, which is advantageous for many applications. This can be accomplished by dividing the processes of nucleation and growth. For instance, you might quickly produce a high supersaturation to generate nuclei, and then you could drop the supersaturation below c_{\min} to stop further nucleation. All of the nuclei are guaranteed to originate under the same circumstances when they are generated simultaneously, which results in similar following growth processes and homogeneous particle size, so in short the growth rate for all the particles will remain same.[12]

2.1.2 Iron Oxide Nanoparticles:

Because of its many uses, iron oxide nanoparticles (IONPs) have gained popularity in a variety of fields, making it easier for high technology based on nanoscale materials to advance. IONPs can be found in different phases including magnetite, hematite, maghemite, and wustite. IONPs can be employed for a wide range of applications [13] including electronics[14], energy [15], biomedicine [16], biotechnology [17], and agriculture [18] due to their high stability, low cost of synthesis, biodegradability potential biocompatibility, and nontoxicity respectively for each application.

The magnetic properties of IONPs are of utmost importance in this research. A detailed discussion on the magnetic properties of IONPs is given below.

2.1.2.1 Magnetic Properties of Iron Oxide Nanoparticles

This section will provide a macroscopic and microscopic description of the theoretical framework for the magnetic characteristics of IONPs. The macroscopic description is about how a material reacts when an external field is applied. When a magnetic field, \mathbf{H} , is applied to a material, the magnetic flux density in that material is given by

$$\mathbf{B} = \mu_0(\mathbf{H} + \mathbf{M}) \quad (2.5)$$

where \mathbf{M} is the material's macroscopic magnetization and μ_0 is the permeability of the vacuum. Vectors are indicated by the bold letters. Since $\mathbf{M} = 0$ in a vacuum, $\mathbf{B} = \mu_0\mathbf{H}$. The quantity N of magnetic moments μ per volume V is known as the magnetization:

$$\mathbf{M} = \mu \frac{N}{V} \quad (2.6)$$

Increased magnetization will arise from a parallel alignment of the magnetic moments, but oppositely aligned moments will cancel one another out. A dimensionless variable that characterizes the magnetization in response to an applied field, susceptibility is defined as $\chi = M/H$ [19].

The arrangement of the magnetic moments connected to the atoms or ions in the crystal lattice controls how magnetic crystalline materials behave. Different sorts of magnetic ordering may occur from how these magnetic moments act collectively. As a result, the material's crystallinity will have a significant impact on its magnetic characteristics.

Because of the electrons' orbital angular momentum L_m and spin S_m , an atom has a magnetic moment, which results in an orbital magnetic moment of μ_l and a spin magnetic moment of μ_s , respectively. The electrons' quantized energy levels lead to the application of a quantum mechanical explanation. The orbital magnetic moment is produced by the electrons precession around the nucleus

$$\mu_l = -\frac{e\hbar}{2m_e} L_m \quad (2.7)$$

where m_e is the electron mass, e is the elementary charge, and \hbar is the reduced Planck's constant.

One way to express the intrinsic electron feature of spin is as follows:

$$\mu_s = -\frac{e\hbar}{m_e} \frac{S}{m} \quad (2.8)$$

The orbital and spin moments are not mutually exclusive but rather interact. The sum of the orbital and spin magnetic moments is the total angular magnetic moment, abbreviated J_m . For the electrons to have a net magnetic moment that does not cancel out, there needs to be an asymmetry

in the electron distribution since the moments have a direction. Therefore, atoms with completely filled electron levels are not magnetic in any way. In the remaining portions of this study, the vector notation not be applied because the vectors' directions won't be taken into account. [19-21]

Magnetite has the chemical formula Fe_3O_4 , in which the O_2^- ions have an outer electron shell that is entirely filled and do not contribute to magnetic properties. Fe_3O_4 has an inverted spinel structure, with half of the Fe^{3+} ions occupying the tetrahedral sites and the other half occupying the octahedral sites in equal numbers. The magnetic moments of the ions occupying the octahedral and tetrahedral sites are antiparallel, canceling out the magnetic moments of the Fe^{3+} ions. The Fe^{2+} ions are now responsible for a net moment. Ferromagnetism (FM) is the term for this magnetic configuration of two sublattices with opposing magnetic orientations but unequal magnetic strengths[20].

An easy axis of magnetization is parallel or antiparallel to the magnetic moments in FM materials. There is an energy barrier that must be crossed to flip the magnetic moment from one direction to the other. The FM alignment is not uniformly distributed throughout the crystal but is instead broken up into domains with distinct axes, the size of which is determined by the equilibrium between the energy of the domain wall and the energy of demagnetization. When a particle is smaller than a particular size, the domain wall energy dominates and causes it to become a single domain. This is thought to be true for magnetite particles smaller than 100 nm. The energy barrier for flipping the magnetic moments gets decreasing as the particle size decreases until it is less than thermal energy at room temperature. In the absence of an external magnetic field, the particle's magnetic moments show zero net measured magnetization due to the ensuing fast thermal fluctuations. It is said to be superparamagnetic [20].

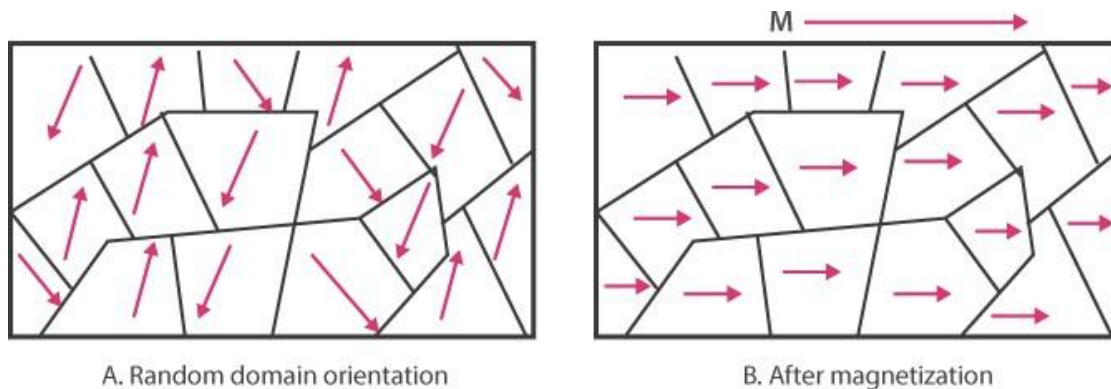


Figure 2-4 Ferromagnetism behavior of materials

As seen in Figure 2.4 , SPM NPs magnetize parallel to an applied magnetic field. The saturation magnetization, M_s , is the greatest value that the magnetization they can achieve. Due to the quick relaxation of the magnetic moments when the field is switched off, there is no remnant magnetization when the field is turned off, as seen by the lack of hysteresis in the curve [21]. Heat is produced as a result of this relaxation.

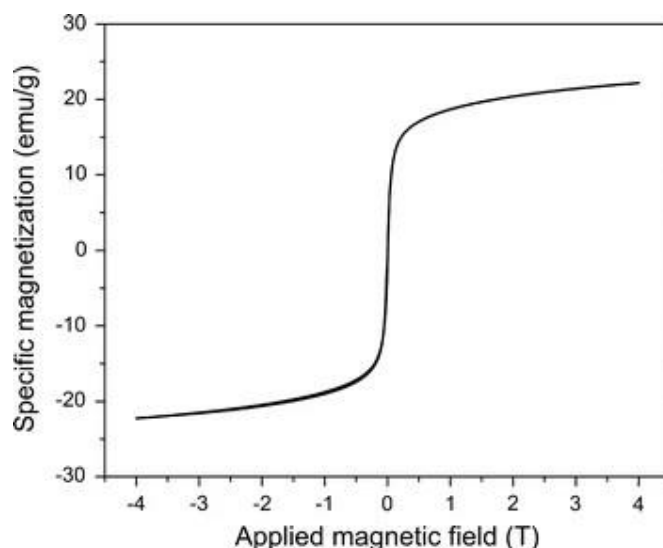


Figure 2-5 The application of an external magnetic field that causes superparamagnetic particles to become magnetized. Saturation magnetization is known as M_s .

2.1.2.2 Synthesis of Iron Oxide Nanoparticles

Interestingly, numerous methods can be used to synthesis IONPs, and the results can vary in terms of shape, size, distribution, chemical stability, and superparamagnetic strengths.

Various methods of IONPs synthesis has been summarized with advantages and disadvantages in table 2.1

Table 2.1 Summary of various methods of IONPs synthesis

Sr. No.	IONPs synthesis methods	Advantages	Disadvantages	Reference
1	Solvothermal	By optimizing the parameters, the final product's size, form distribution, and crystallinity may be easily and precisely controlled.	The requirement for costly autoclaves. Problems with safety throughout the reaction.	[24-27]

2	Sonochemical	It has the ability to create SPIONs with precise sizes and shapes, strong crystalline affinity, minimal energy consumption, and excellent stability.	Temperature control in ultrasonic baths is a very challenging task. This is due to the fact that ultrasonic baths typically cause an uneven temperature distribution when they are in use since they warm up.	[28, 29]
3	Hydrothermal	Particle shapes and sizes can be manipulated by varying the hydrothermal conditions and starting materials.	Prior understanding of initial material solubility is necessary.	[30-32]
4	Sol-gel	Superior control over the stoichiometry and chemical homogeneity of the precursor, ease of integration of a broad variety of functional groups, relatively short annealing time, control over nanoparticle size, and low temperature crystallization.	Compared to other fabrication techniques, sol gel requires more time due to its slow gel formation process.	[33, 34]
5	Thermal decomposition	The monodispersity is enhanced by using thermal breakdown, and the IONPs' size and form can be adjusted.	The main problem with IONPs produced from thermal degradation is that they are frequently hydrophobic and only dissolve in organic solvents that are non-polar. Phase transfer from the organic to the aqueous phase is required to get around this.	[35]

There is another method known as co-precipitation method that has been widely used because its The manufacture of thin metal oxide powders, which are highly reactive in low temperature sintering, can be done simply and directly.

It is mostly commonly used method as has ben adapted in this thesis.

2.1.2.3 Stability and Functionalization of IONPs

IONPs are readily oxidized by ambient oxygen, leading to a notable decrease in their magnetism and dispersibility[35, 37, 38]. This means that in order to enhance IONPs' dispersibility in water, safeguard therapeutic agents from deterioration, and significantly impact the biokinetics and biodistribution of IONPs within the organism, biofunctional coatings must be developed[39, 40].

The IONPs can be coated with different materials such as polymers. According to Arias et al.[41], such systems have the potential to be associated with several drug classes for biomedical applications. Adsorption, dispersion in the polymer matrix, encapsulation, electrostatic interactions, and covalent attachment to the surface are some of the mechanisms by which these drug classes can be connected. Furthermore, such nanoparticles might be functionalized with organic substances such as ligands that have the potential to be used in cancer detection and therapy. For IONPs, coatings come in two varieties: organic and inorganic. The benefits of the organic and inorganic coatings in IONPs are presented in Table 2.2. [42]

Table 2.2: Advantages of organic and inorganic coatings on IONPs

Coating	Advantages
Inorganic	Helps molecules to get functionally bonded to one another and avoid clumping. enhances stability, hydrophilicity, and biocompatibility.
Organic	Can produce amphiphilic, oil- or water-soluble nanoparticles, depending on the kind of organic molecule or surfactant that is utilized.

Polymer coatings improve biocompatibility and bioavailability.

In biological applications, organic coatings have been applied for controlled drug release. They also improve the biocompatibility and dispersibility of IONPs. To create organic coatings for IONPs, a number of techniques (post-synthesis and in situ) have been devised [35]. Three categories apply to organic coatings: (1) biological molecules; (2) macromolecules and polymers; and (3) tiny molecules and surfactants[43].

I. Biomolecules

Highly biocompatible are the IONPs functionalized with biomolecules (enzymes, proteins, antibodies, biotin, avidin, human/bovine albumin, and polypeptides, among others). [43]. Furthermore, green synthesis can be used to functionalize IONPs [44], Aloe vera nanocellulose, which has demonstrated antibacterial activity, is another substance that has been utilized lately for green production and coating IONPs that are 15–30 nm in size [45].

II. Polymers

The most researched coatings are made of polymers like polyethylene glycol (PEG), polyvinyl alcohol (PVA), polymethyl methacrylate (PMMA), and polylactic acid (PLA). In order to prevent

particle aggregation, the polymers produce steric effects and electrostatic forces of repulsion [40, 43]. Additionally, coatings using smart polymers that react to light, pH, temperature, and other stimuli have been tested [46]. However, under some circumstances, the presence of polymers may alter the magnetic characteristics of IONPs [37], these characteristics may be related to spin canting, particle interactions, or modifications in the particle size distribution.

To create nanoparticles that can be used to treat cancer, natural polymers such as dextran, chitosan, gelatin, and starch are frequently utilized. According to Barrow et al. [47] and Ebrahimi [48], these polymers serve as stabilizers during the synthesis process to improve the stability, biocompatibility, and biodegradability. Avazzadeh et al. [49], for instance, functionalized IONPs with dextran-spermine to treat breast cancer by inducing hyperthermia. After a 20-minute treatment cycle, approximately 63% of cancer cells were killed, confirming the ability of nanoparticles to target cancer cells and heat them to hyperthermia. Furthermore, Nguyen [50] coated IONPs with gelatin; the IONPs were made using the coprecipitation process and functionalized with paclitaxel, exhibiting a consistent and prolonged release profile in vitro for a maximum of five days.

III. Small molecules and surfactants

Surfactants enhance the stability, dispersibility, and biocompatibility of IONPs. Additionally, they are classified into three subclasses based on their nature: amphiphilic, water-soluble, and oil-soluble surfactants. They can also be employed as coatings [51].

Hydrophobic groups are present in oil-soluble surfactants, which are employed in oily solutions to promote stability and inhibit agglomeration. These nanoparticles also have a variety of uses, including as MRI contrast agents and drug transporters in certain drug delivery systems [43].

In situ functionalization of hydrophilic IONPs with short-chained surface coating molecules (containing at least two carboxyl functional groups) was described by Kandasamy et al. [52]. These nanoparticles have the potential to serve as efficacious nanomedicines for the treatment of cancer. Additionally, Zhao et al. [53] used WO_3 , Fe_3O_4 , and 3-aminopropyl triethoxysilane to create a multilayer structure. VP16 was delivered and released under control using IONPs, which were synthesized by thermal degradation and microwave irradiation.

A. Oleic Acid Functionalization

The purpose of this study is to co-encapsulate hydrophobic IONPs and Paclitaxel in PLGA. Functionalization with oleic acid has been reported to impart hydrophobicity in IONPs. As shown

in Figure 2.4, oleic acid is an amphiphilic molecule consisting of two components: a non-polar hydrophobic chain and a polar hydrophilic head group. The oleic acid is soluble in water and polar solvents due to its polar head, and it is soluble in petroleum and non-polar solvents due to its hydrophobic tail. Since water will be used as antisolvent in flash nanoprecipitation and THF as solvent(explained in detail in 2.1.3.1), this characteristic of oleic acid is of crucial importance here. Many features are determined by the relative sizes of the two groups [54, 55].

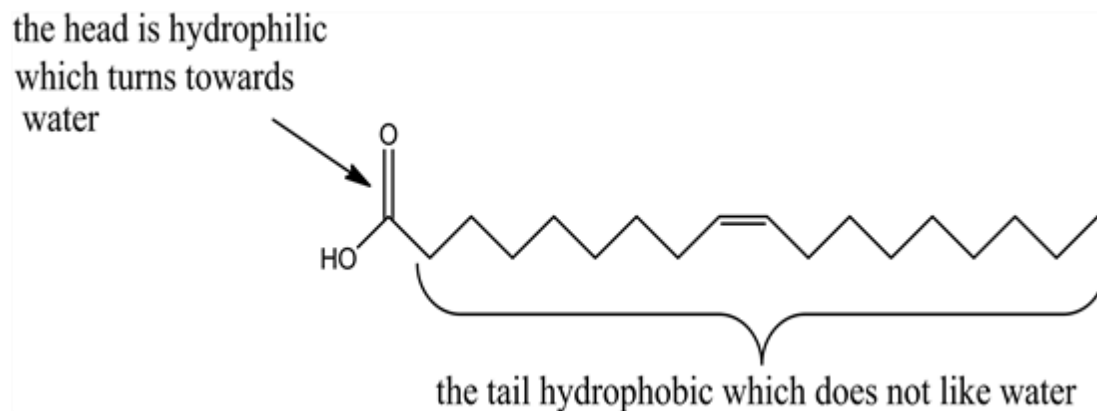


Figure 2-1 Structural formula of oleic acid

2.1.3 Methods for Polymer coating of IONPs

Many methods for coating/encapsulation of IONPs by polymer has been reported in literature. Some of those methods are summarized below.

Table 2.3: Methods for coating/encapsulation of IONPs by polymer

Technique	Description	Reference
In Situ Polymerization	Synthesis of polymer-coated IONPs during nanoparticle synthesis process.	[56, 57]
Surface Modification	Functionalized polymers are attached to IONP surface via covalent or non-covalent interactions.	[58][61]
Solvent-evaporation method	Solvent evaporation involves two steps: emulsifying the polymer in the aqueous phase and dispersing it in a volatile solvent like dichloromethane, chloroform, or	[59]

	ethyl acetate. Subsequently, the solvent is evaporated through the use of high temperature, vacuum, or constant stirring. It has been extensively studied for coating of IONPs.	
Emulsion Polymerization	Monomer polymerization occurs within emulsion droplets containing IONPs.	[60]
Ligand Exchange	Polymer chains adhere to IONP surface by ligand exchange	[62]
Microfluidic Synthesis	Precise control over synthesis and coating of nanoparticles using microfluidic devices.	[63]

Recently a lot of research is being done on the solvent displacement methods. The solvent displacement methods, especially the flash Nanoprecipitation, allow for fast one step homogeneous NPs synthesis. Furthermore, the process allows ease of drug addition compared to indirect methods[64-66].

2.1.3.1 Concept of Flash Nanoprecipitation

The solvent displacement method is a straightforward, one-step way of producing polymeric nanoparticles. Dimethylsulfoxide (DMSO), tetrahydrofuran (THF), acetone, or methanol are examples of common organic solvents. The traditional approach to solvent displacement uses the nanoprecipitation technique, which involves injecting droplets of the organic solvent into a vial that already contains the stirring antisolvent in bulk. The arrangement allows for the synthesis of a variety of polymeric nanoparticles without the need for a specialized reactor. The wide particle size distribution that results from the standard nanoprecipitation method's lack of control during mixing (using a stirring bar as a mixer) is a significant disadvantage. [66, 67].

These problems are addressed by the addition of a mixing chamber for the polymer-containing solvent and the anti-solvent in the flash nanoprecipitation (FNP) method, which was first developed by Brian K. Johnson and Robert K. Prud'homme [68]. The main process is the high-speed, millisecond-short mixing-interval injection of the solvent and anti-solvent through two or more inlets into a specific reactor. The two streams are moved toward the reactor at the desired rates using syringe pumps. The two types of reactors now in use are the confined impinging jet

(CIJ) [68] and the multi-inlet vortex mixer (MIVM) [69] (Figure 2.5). The potential ratio between the two mixing solutions is the main distinction between the two geometry types. There can only be two equal-flow inlets for the CIJ. By including inlets to the design and adjusting the solvent/anti-solvent ratio, the MIVM is well scalable and can overcome the pump limits. Rapid turbulent mixing inside the reactor causes local supersaturation and the emergence of polymer nanoparticles. The size of the NPs that are produced is directly influenced by variables like flow rates and solvent/anti-solvent ratios during the kinetically controlled production process. Additional components, such as anti-cancer medications and fluorescent polymers, can be added to the solvent or anti-solvent for biomedical purposes. To create multifunctional polymer NPs, these elements can be incorporated inside or added to the coating. One outlet removes the product from the reactor. Additionally, this procedure is easily scaled up to industrial scale for the synthesis of substantial amounts of nanoparticles [70, 71].

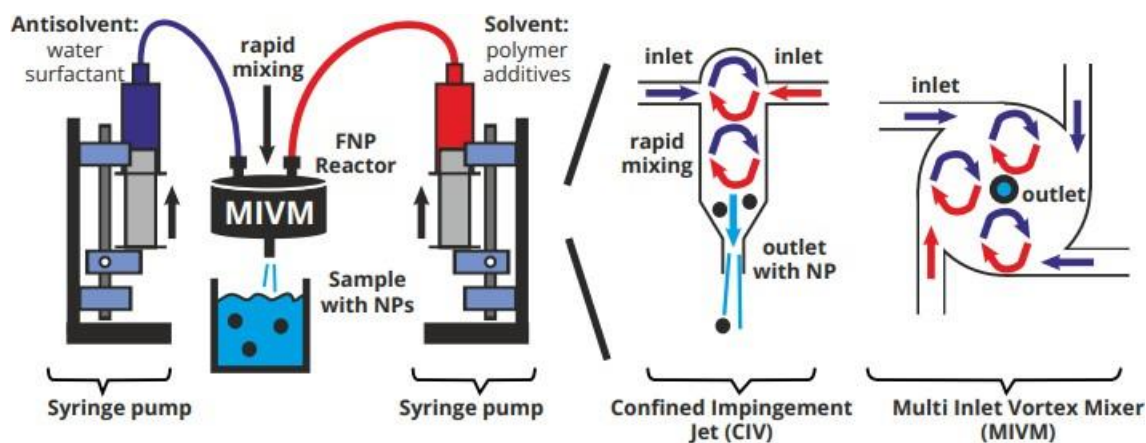


Figure 2-6 Flash nanoprecipitation setup and common reactor types (confined impingement jet (CIJ) and multi inlet vortex mixer (MIVM))

I. Nucleation and growth theory of particle formation in FNP

The solute concentration (C) divided by the equilibrium solubility concentration (C^*) yields the supersaturation (S) value. After the system reaches supersaturation, solute particle nucleation drives system evolution. The solute concentration decreases as a result of nuclei forming, and this facilitates the growth mechanism by means of diffusion to previously created particles. The main mechanism is the growth and aggregation of already created particles; below C_{\min} , no new particles are formed in the solution.

The development of the particle by solute addition is halted when the solute concentration reaches the equilibrium solubility concentration. Stabilizing agents can be added to the solution to stabilize the generated NPs[10].

$$S = C/C^* \quad (2.9)$$

The La Mer mechanism explains how the polymeric NPs are formed during the flash nanoprecipitation procedure. In a restricted reactor (Stage I) (Figure 2.6), an organic solvent containing the polymer solute collides with an antisolvent at extremely high speeds[71, 72]. The two streams combine turbulently in a few of milliseconds. The hydrophobic solutes and the polymer directly reach a supersaturated concentration in the antisolvent around the critical limiting supersaturation (C_{max}) (Stage II) from the organic phase. The concentration of the solute rapidly drops and a large number of monodisperse nuclei are generated. The remaining hydrophobic solutes interact with the surrounding produced nuclei to cause the particles to expand (Stage III). The induction time for nucleation and growth ($t_{nuc,gro}$) must be longer than the mixing time (t_{mix}) of the two miscible liquids in order to produce monodisperse particles. This permits nucleation to take control of the process. In this instance, the particle size is not defined by diffusion-limited growth. Similar to this, in order to prevent a notable rise in particle size and polydispersity, the induction time for the diffusion-limited aggregation of the particles must be longer (t_{agg}) than the mixing time. The interplay between polymer and polymer as well as size and number-density determine the true aggregation behavior.

Stabilizing the generated NPs will control cluster-cluster aggregation. As long as an amphiphilic layer from a surfactant or block copolymer stabilizes the nanoparticles after this point, the solvent/antisolvent mix reaches equilibrium solubility and the particle size remains constant.

The nucleation rate (J) can be utilized in Equation (3) to gain a deeper understanding of the nucleation during FNP. In FNP, a monodisperse distribution of NPs is obtained by a high nucleation rate. Temperature (T), surface tension (γ), molar volume (v), and supersaturation (S) all directly affect the nucleation rate. The rate of nucleation rises with increasing supersaturation, which makes it easier for more monodisperse nuclei to form. The characteristics of the resultant polymer NPs are significantly impacted by changes in mixing duration and solute concentration. [10, 71, 72]

$$J = A \exp \left[- \frac{16\pi\gamma^3 v^2}{3(k_B T)^3 (\ln S)^2} \right] \quad (2.10)$$

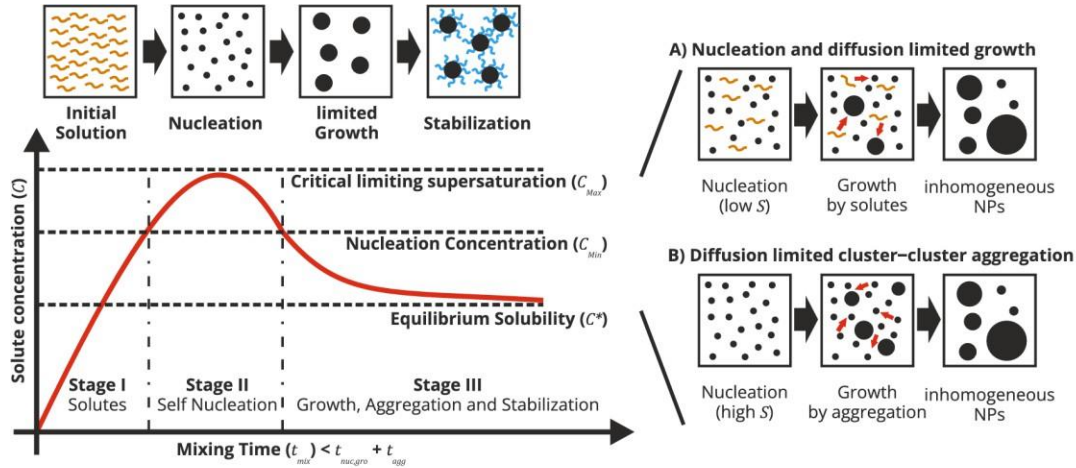


Figure 2-7 La Mer Diagram: formation of NPs through Supersaturation (S) in FNP reactor.

II. Polymer particle stabilization

The process of polymeric NP synthesis in FNP is kinetically regulated. There is hydrophobic contact between the NPs, and the resulting NPs are not very stable. There are two approaches that can be used to stabilize and stop aggregation. The amphiphilic block-copolymer's hydrophilic portion (such as PEG) can attach to the water molecule and create stable core-shell structures. Here, the PEG inhibits development by stabilizing the hydrophobic core and protecting it from an adverse contact with water[73, 74].

To stop the hydrophobic polymer and medication structure from clumping together and precipitating, further stabilizing agents in the form of amphiphilic structures can be added to the antisolvent.

The hydrophobic portion of the amphiphilic stabilizer bonds with the hydrophobic polymeric NPs structure during particle production in FNP, protecting it from adverse interactions with water molecules. This mechanism also prevents the particles from growing any further at the same time. Polysorbates and PVP are common NPs stabilizers for FNP. The additional stabilizers must be authorized biocompatible compounds[10].

III. Parameters influencing the FNP process

The size and size distribution of the resulting polymeric NPs can be controlled by varying the kinetic parameters of the particle formation.

Polymer concentration

The size of the resultant polymeric NPs is strongly influenced by the concentration of polymer in the solvent. Equation shows that when the polymer concentration rises, the supersaturation and nucleation rate both rise. Greater interaction between the polymers results from an increase in the number of nuclei in the sample. This encourages aggregation [71]. To prevent the aggregation of hydrophobic polymers or therapeutic agents in FNP systems, amphiphilic polymers or stabilizing agents are needed. By decreasing the particle size and preventing future development through aggregation, the stabilizing agent's concentration can be increased[10].

Molecular weight

The molecular weight of an amphiphilic block-copolymer does not significantly affect the size of the formed polymer NPs [75]. However, by adding hydrophobic molecules with higher molecular weight, an increase in the size of resulting particles is observed. Changes in the supersaturation, the number of nuclei formed as well as in the interaction between the polymers contribute to the increase [76].

Flow Rate/Solvent to Antisolvent Ratio:

The Reynolds number (Re) has a direct correlation with the flow rate's effect on the size of the resultant nanoparticles. Equation provides an approximative definition of Re for the MIVM. The volumetric flow rate (V_i) multiplied by the reactor's diameter (L) and divided by the associated stream's kinematic viscosity (ν_i) yield the Re for each inlet (i). The viscosity (η_i) of the liquid divided by the density (ρ) yields the kinematic stream viscosity [77].

$$Re = \sum_{i=1/N} \frac{V_i * L}{\nu_i}, \nu_i = \frac{\eta_i}{\rho_i} \quad (2.11)$$

Type of Polymer:

The solubility of polymers can vary based on their chemical structure. Molecular models such as the Hoy solubility parameter (δ_{Hoy}), the Hansen solubility parameter (HSP), or the Hildebrand solubility parameter (δ_{HISP}) can be used to express the solubility. The latter two precisely determine a polymer's overall solubility by utilizing three distinct factors for hydrogen (δ_H), polar (δ_P), and dispersion (δ_D) interactions[74, 75].

$$\delta_{HISP}^2 = \delta_D^2 + \delta_P^2 + \delta_H^2 \quad (2.12)$$

Lowering the polymer's total solubility in the antisolvent causes the supersaturation to rise and the particle size to decrease. When dealing with block-copolymers, it is necessary to take into account the solubility of each polymer block independently. The hydrophilic domain becomes trapped in the hydrophobic core due to similar solubility parameters, which lessens the hydrophobic core's

shielding and decreases the stability of the nanoparticle. Larger particles are formed by the dissolution and addition of polymer as a result of Ostwald ripening, which is brought on by the diffusion of entrapped hydrophilic domains to the particle surface. The ability of the polymer to form stable particles can also be influenced by its thermal characteristics. High polymer mobility in the NPs' core and particle aggregation can result from low melting (T_m) and/or glass transition (T_g) temperatures [75].

Solvent

The polymer's solubility varies with different solvents, which modifies the reaction's supersaturation conditions. Diffusion is higher in some solvents than in others. It is evident that an increase in Ostwald ripening reduces the stability of the NPs. Via dialysis or vacuum evaporation, the organic solvent may be removed[72, 74].

Hydrophobicity:

When coating hydrophobic substances with polymeric nanoparticles, the loading of such entities within the polymer is thought to be related to variations in the kinetics of their nanoprecipitation, which in turn rely on the hydrophobicity of the entity. If the entities being loaded are highly hydrophobic in comparison to polymer, it will have the time to embed into the forming polymeric nuclei at the very beginning of the particle growth. In order to start the development of particles, the entities can also form nuclei or at least take part in their formation. The production of nanoparticles (NPs) with a highly concentrated load within their core relative to the remainder of the particle could be explained by one of the two possibilities. Andreas et al. have explored this for polymers with different hydrophobicity in comparison to the dye being loaded[78].

2.1.4 Polymer coated Iron oxide nanoparticles for theranostics

Polymer-coated iron oxide nanoparticles (IONPs) hold promise for various applications in cancer treatment due to their unique properties, such as biocompatibility, tunable surface chemistry, and magnetic responsiveness. Here's an overview of how polymer-coated IONPs are utilized in cancer treatment:

2.1.4.1 Drug Delivery:

Polymer coatings can be functionalized with targeting ligands and loaded with chemotherapeutic drugs or therapeutic agents. These functionalized IONPs can selectively accumulate in tumor tissues through passive or active targeting mechanisms, minimizing off-target effects and

enhancing therapeutic efficacy. Additionally, the magnetic properties of IONPs enable targeted drug delivery through the application of external magnetic fields.

2.1.4.2 Hyperthermia Therapy:

When exposed to an alternating magnetic field, polymer-coated IONPs generate heat through magnetic relaxation processes. This localized heating effect can be exploited for hyperthermia therapy, where elevated temperatures selectively induce tumor cell death while sparing healthy surrounding tissues. The polymer coating helps stabilize the IONPs and improve their biocompatibility during hyperthermia treatment.

One minimally invasive treatment for hyperthermia is the use of magnetic fluid as a source of heat.[79] A stable colloidal suspension of magnetic nanoparticles (MNPs) scattered across an aqueous medium is referred to as a magnetic fluid. A magnetic fluid is a stable colloidal suspension [80] of magnetic nanoparticles (MNPs) dispersed in an aqueous medium. The heating efficiency of magnetic colloids is typically quantified through the specific absorption rate (SAR) The specific absorption rate (SAR) is calculated using the following equation,

$$SAR = C \frac{\Delta T}{\Delta t} \frac{1}{m_{Fe}}$$

where C is the specific heat of solvent (here $C_{water} = 4.18 \text{ J/g}^\circ\text{C}$), $\frac{\Delta T}{\Delta t}$ is the initial slope of the time-dependent temperature curve and m_{Fe} is the weight fraction of magnetic element (i.e. Iron Oxide) in the sample.[81]

2.1.4.3 Magnetic Resonance Imaging (MRI):

In addition to therapeutic applications, polymer-coated IONPs are used as contrast agents for MRI. Their magnetic properties induce changes in signal intensity, allowing for the non-invasive visualization and monitoring of tumors *in vivo*. The polymer coating ensures the stability and biocompatibility of the contrast agent during imaging procedures.

2.1.4.4 Photothermal Therapy (PTT):

By incorporating photothermal agents into the polymer coating, IONPs can absorb near-infrared light and convert it into heat, leading to localized thermal ablation of tumor tissues. This combination of magnetic and photothermal properties enables synergistic therapeutic effects and precise control over the treatment site.

2.1.4.5 Radiotherapy Enhancement:

Polymer-coated IONPs can also enhance the efficacy of radiotherapy by sensitizing tumor cells to ionizing radiation. When internalized by cancer cells, the IONPs interact with radiation beams, generating reactive oxygen species and DNA damage, thereby increasing the effectiveness of radiotherapy while minimizing damage to healthy tissues.

Overall, polymer-coated IONPs represent a versatile platform for cancer treatment, offering multifunctionality, targeted delivery, and imaging capabilities that hold great potential for improving therapeutic outcomes and reducing side effects in cancer patients.

A summary of some break through research papers in this field has been given below in Table 2.4

Table 2.4 Summary based on literature survey for Polymer coated Iron oxide nanoparticles for cancer treatment

Author	NPs	Polymer Modification	Drug	Cancer Cell Line	Conclusions (Refs.)
Mangaiyarkarasi et al.	Fe ₃ O ₄ @LaF ₃ :Ce ³⁺	Chitosan	Paclitaxel (PTX)	A549	Greater cytotoxic effect on A549 lung cancer cell lines in contrast to free PTX. [82]
Situ et al.	SPION	Dextran (DEX), PLGA and micelle	Doxorubicin (DOX)	BEL-7402	The efficient delivery of the nanocarrier to the tumor tissue and its potential for tailored tumor targeting and effective tumor therapy are noteworthy. [83]
Menon et al.	SPION	Chitosan and (PLGA)	—	A549, H460	Showed that a treatment was beneficial by decreasing the growth of the tumor. [84]

Feng et al.	SPION	PEG	—	BALB/c mice	Potent cytotoxicity, rapid absorption by cells, quick elimination, and narrow distribution of tumors. [85]
Albukhaty et al.	SPION	DEX	Vinblastine (VBL)	PANC-1	Long-lasting release profile, dose- and time-dependent targeted cancer cell cytotoxicity, and more potent tumor growth inhibition in PANC-1.[86]
Mahdi et al.	SPION	DEX	5-fluorouracil (5-FU)	SNU-423	Excellent biocompatibility, excellent loading efficiency, controllability, penetrability, and growth-inhibiting effectiveness against tumors.
Al-Kinani et al.	Fe@Au	Chitosan (CS)	—	T-47D	Decrease in T-47D cell viability due to significant increases in apoptotic levels. verified the average tumor size's gradual decline to a minimal size [88].
Senturk et al.	SPION	PLGA-b-PEG	CU	GBM	Shown toxicity to T98G cells, which had a viability rate of less than 16%. The engineered MNPs have a controlled 72-hour release window for 70% of their pharmacological load [89].

Al-Musawi et al.	SPION @Au	Chitosan	DOX	SkBr3	When compared to mice given the free medication, in vivo studies showed that the development of tumors was markedly suppressed in the mice given this nanocarrier. [90]
Adawiya et al.	Fe ₃ O ₄ @Au	Chitosan (CS)	CU	MDA-MB-231	When compared to an unloaded nanocarrier, the nanocarrier exhibits a discernible enhanced effect in cell death and apoptosis induction. It also induces an increase in MDA-MB-231 cell death, which results in an 18.5% apoptosis rate.[91]
Bahjat et al.	Fe ₃ O ₄ /TiO ₂	—	DOX	A549	When it comes to lung cells (A549), the nanocarrier is more cytotoxic than when it comes to the normal cell line (WRL-68).[92]

CHAPTER 3: MATERIALS AND METHODS

3.1 Materials

Iron (II) Chloride FeCl_2 , Iron (III) chloride FeCl_3 , Ammonia solution 25%, Oleic acid, Tetrahydrofuran (THF), Absolute Ethanol and Polysorbate 80 were purchased from Sigma Aldrich. Poly Lactic-co-Glycolic Acid (PLGA) was purchased from Evonik. All the chemicals were used as received. For all the experiments, Mili-Q water with resistivity $18.2 \text{ M}\Omega \cdot \text{cm}$ was used.

In the following sections, synthesis methods of IONPs and their coating with oleic acid, oleic acid coating optimization, synthesis of bare polymeric particles followed by synthesis of polymer coated IONPs will be discussed.

3.2 Synthesis of Oleic acid coated Iron Oxide Nanoparticles

3.2.1 Method I.

Iron oxide nanoparticles were synthesized by co-precipitation method using ferric 2.7g (0.1 mole) and ferrous chloride 1.0g (0.05 mole) salts at 2 : 1 molar ratio of Fe^{3+} : Fe^{2+} as shown in the figure 3.1 After dissolving ferric and ferrous chloride in 100 milliliters of water, 15 milliliters of ammonium hydroxide were added while the mixture was continuously mechanically stirred at 425 revolutions per minute. After that, the reaction mixture was heated to 80°C . To coat the iron oxide nanoparticles, known as OA-IONPs, with oleic acid, 10 mL of oleic acid was added to the reaction system. The reaction mixture was then mechanically agitated for an additional two hours. The nanoparticles were then magnetically separated and rinsed three times with a 50% ethanol/water solution. Following the removal of the supernatant, IONPs were dispersed in THF. This method was adopted from the work Rashid M. et al. [93] and the washing steps and dispersion in THF were modified.

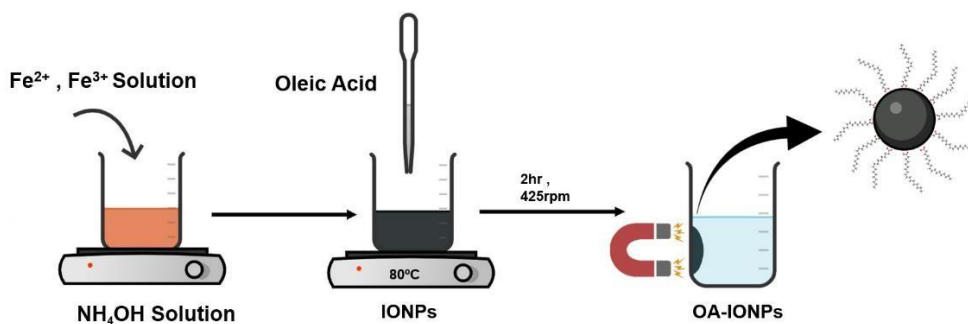


Figure 3-1: Synthesis of oleic acid coated Iron oxide nanoparticles

3.2.2 Method II.

Iron oxide nanoparticles were synthesized by co-precipitation method using ferric 10.80g (0.1 mole) and ferrous chloride 4.00g (0.05 mole) salts at 2: 1 molar ratio of Fe^{3+} : Fe^{2+} . Ferric and ferrous chloride were dissolved in 50 mL of water. 15.4 mL of 25% of ammonium hydroxide was added in 84.6 ml of water. 10 mL of salts solution was added three drops per second with the help of a burette in Ammonia solution at magnetic stirring of 380 rpm. The nanoparticles were magnetically separated and washed with water three times. The supernatant was removed and IONPs were redispersed in water.[94] For 200 mg of IONPs dispersed in water, 1.2 ml of oleic acid was added and sonicated at 67 °C for two hours. After two hours, oleic acid coated IONPs were magnetically separated and washed with 50% ethanol-water three times and dispersed in 5ml THF. Fig 3.2 shows the schematic of the process.

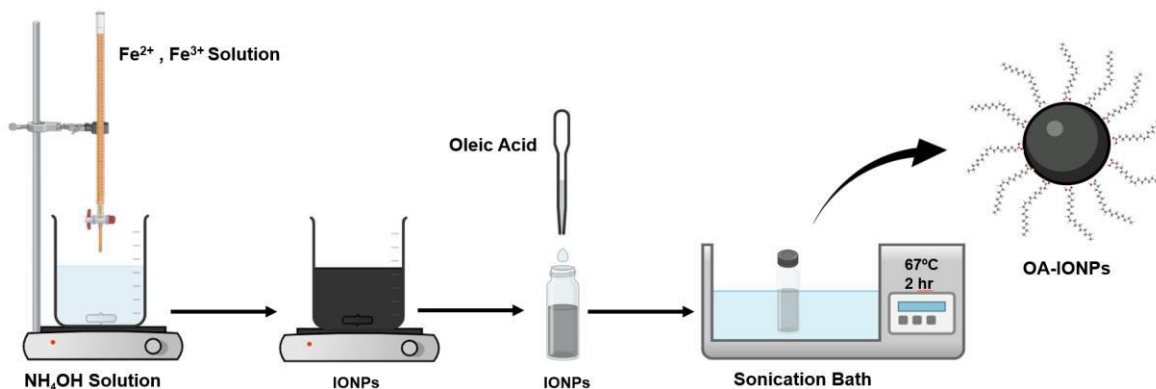


Figure 3-2: Synthesis of oleic acid coated Iron oxide nanoparticles

3.3 Optimization with different amounts of Oleic acid

The functionalization process of iron oxide nanoparticles for method II was optimized for different volumes of oleic acid. 0.4 ml, 0.5 ml, 0.6 ml, 0.8 ml, 1.0 ml and 1.2 ml of oleic acid was used for each 200 mg IONPs sample dispersed in water. All the samples were sonicated at 67 °C for two hours. After two hours, oleic acid coated IONPs were magnetically separated and washed with 50% ethanol-water three times and dispersed in 5ml THF.

3.4 Synthesis of PLGA nanoparticles

PLGA nanoparticles were made by flash nanoprecipitation, work adapted from Saad et. al. [95] 192 mg PLGA was dissolved in THF (organic phase) by magnetic stirring at 200 rpm for 5 minutes. In a volumetric flask 0.1 W/V.% Tween 80 solution in water was prepared (aqueous phase). With the use of infusion pumps, organic and aqueous phases were introduced in the two-inlet MIVM flash nanoprecipitation reactor at the flowrate of 10 mL/min and 100mL/min respectively. After establishing a flow equilibrium throughout the first 30s of the reaction, three samples of 5mL each, were collected at the intervals of 5s

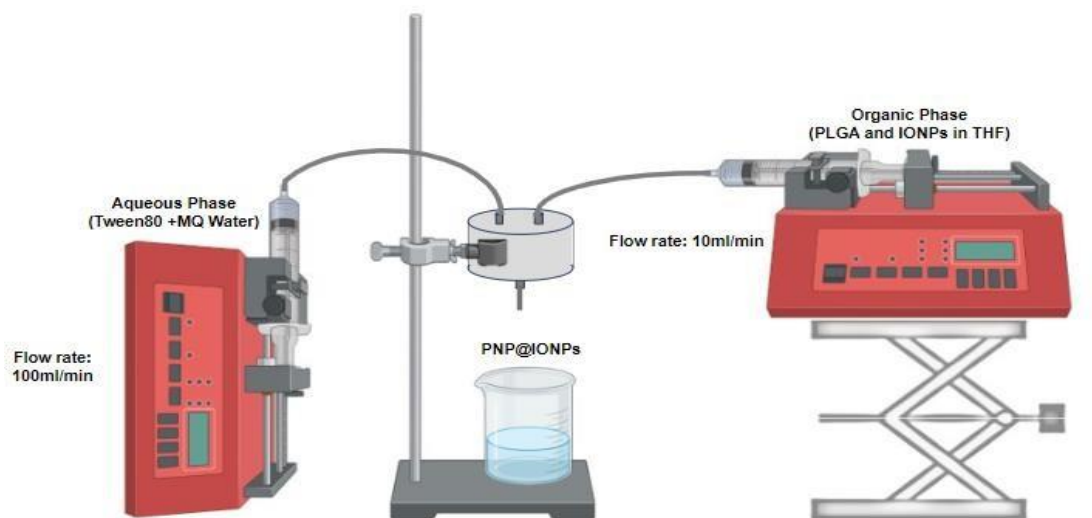


Figure 3-3:Flash nanoprecipitation setup

3.5 Synthesis of PLGA coated Iron Oxide nanoparticles

For PLGA coated IONPs the above procedure was followed with slight modifications. PLGA was dissolved in THF (organic phase) by magnetic stirring at 200 rpm for 5 minutes. This was followed by the addition of OA-IONPs dispersed in THF. The solution mixture was vortexed for 30 secs. In

a volumetric flask 1 wt.% Tween 80 solution in water was prepared (aqueous phase). With the use of infusion pumps organic and aqueous phases were introduced in the two-inlet MIVM flash nanoprecipitation reactor at the flowrate of 10 mL/min and 100mL/min respectively. After establishing a flow equilibrium throughout the first 30s of the reaction, the sample was collected. A quick 30 seconds magnetic separation was done to remove free Iron oxide nanoparticles. Then, the sample was purified by centrifugation, 3x at 8000 rpm using water as solvent.

3.6 Optimization with different PLGA and IONPs concentrations

The polymer coated IONPs are later to be used for biomedical applications, so it is important to control and optimize the size of these particles. Bare PLGA nanoparticles were synthesized for 1, 1.5 and 2 wt% using the same method mentioned above. Then for the optimum wt. % of PLGA, the concentration of Iron oxide nanoparticles was varied from 1 mg/ml to 6 mg/ml.

3.7 Methods for the characterization:

Following Characterization techniques were used.

3.7.1 Fourier-Transform Infrared-Attenuated Total Reflection (FTIR):

The way FTIR spectrometers operate is that infrared (IR) light passes through the crystal and is fully reflected inside at the contact between the crystal and the sample before arriving at the detector. An absorption spectrum unique to each molecule bond is produced by the light absorbed by the molecules in the infrared spectrum. The frequency is measured within the region of 4000-500 cm^{-1} . The energy gap determines the frequency of the absorption peak. This occurs when molecules absorb a certain wavelength of radiation, which excites them and shifts their energy level from the ground state to the excited state.

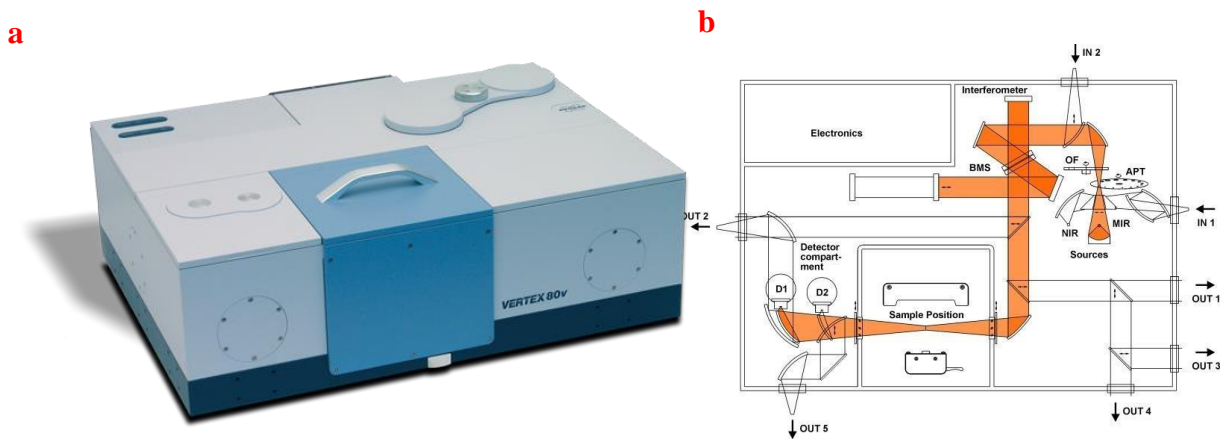


Figure 3-4(a) Bruker Vertex 80v FTIR Spectrometer (b) Schematic showing the main components of FTIR

For this thesis, Thermo Scientific Nicolet iS50 FT-IR with a golden gate diamond attenuated total reflectance (ATR) module was used. 5mg of sample powder was placed on the ATR crystal and screwed down with a cone geometry until a good signal was received. A method with 2cm^{-1} resolution and 100 scans was used. Afterwards the sample was removed, and the crystal was cleaned afterwards with ethanol.

3.7.2 Thermogravimetric analysis (TGA):

Thermogravimetric analysis (TGA) is used to determine the degradation temperature of materials. The main principle is the continuous measure of decreasing mass with respect to the temperature.

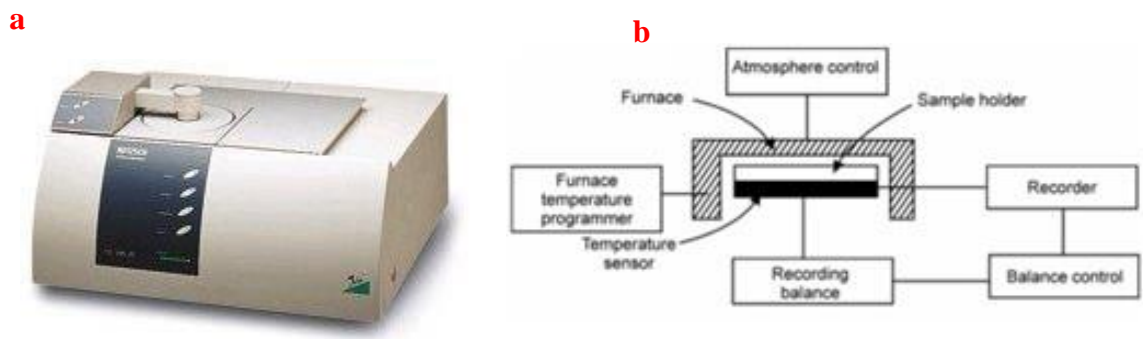


Figure 3-5(a) Netzsch TG209F1 TGA (b) Schematic of components of TGA

The TGA for all polymer samples was performed by weighing 10mg of dried sample into the flame cleaned platinum crucible. For Analysis in Netzsch TG209F1 the sample was heated at a

rate of 20°C/min from 100°C to 1000°C and afterwards cooled with 30°C/min back to room temperature. The crucible was cleaned by holding it into the flame of a heat gun for 1min.

3.7.3 *Dynamic Light Scattering (DLS):*

The Brownian motion of scattered particles is the foundation of dynamic light scattering (DLS). Particles scattered in a liquid flow arbitrarily in every direction. Particles move as a result of the energy that is imparted during these collisions. Smaller particles are more affected by the energy transfer since it is more or less constant. Smaller particles are therefore travelling faster than larger particles. By measuring the particle's speed, you can ascertain the hydrodynamic diameter if you are aware of all other factors that affect particle movement.



Figure 3-6: Anton Paar LiteSizer 500

Bare and Oleic acid coated IONPs were alternatively vortexed and sonicated three times and 1 ml of the sample was taken in disposable cuvette for bare and quartz cuvette for oleic acid coated IONPs on the same instrument settings mentioned above. Zeta potential for the NP solution was measured in an OMEGA® 28 cuvette. The bare polymeric nanoparticles produced by FNP were directly analyzed and polymer encapsulated IONPs were washed three times with water and analyzed in the DLS (Anton Paar Litesizer 500) apparatus. 1 ml of FNP NPs with 10X dilution were filled into a capped polystyrene disposable cuvette and the hydrodynamic size measurement was started (25°C, max. 60runs @10s, automatic). Afterwards the cuvettes were flushed three times with 10mL MQ water to remove the previous sample.

3.7.4 *Scanning Transmission Electron Microscope S(T)EM:*

There are two primary types of signals that can be detected in S(T)EM one is transmitted electrons and the second one is scattered electrons. The transmitted electrons pass through the atom without interaction with the atom and are used to create a high-resolution image of the internal structure of samples. The electron beam interacting with the atoms in the sample, causes them to scatter or absorb some of the electrons, depending on their atomic number and thickness. The scattered and transmitted electrons are detected by a series of detectors positioned above and below the sample. The signal from the detectors is then processed to generate an image of the sample with very high resolution and contrast, revealing the detailed atomic structure of the material. The detectors present in the S(T)EM are specialized detectors which include bright-field detectors, dark-field detectors, high-angle annular dark-field detectors. These detectors help in creating a range of images and analyses of samples.

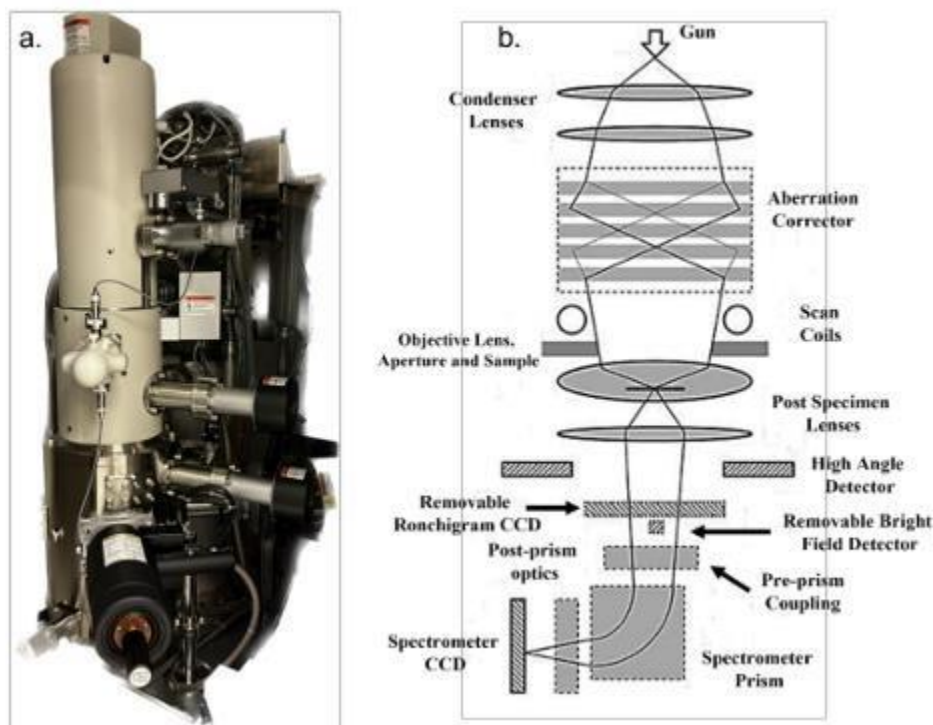


Figure 3-7 (a)High resolution S(T)EM Components (b) Schematic showing the main components of S(T)EM

Grids were prepared such that 10 μ L of the NP suspension were placed on the carbon grid with a mechanical pipette. For IONPs the grids were left to dry for 2 minutes and blotted with wet tissue paper. For PNPs and PNPs@IONPs the grid was left to dry for 30min, and residual sample was removed by a wet tissue paper. Next, 6 μ L of 1% phosphotungstic acid (PTA) stain (pH~7.0) was placed on the grid and left for ~1min before being removed by a wet tissue. Grids were then

analyzed with a NTNU NanoLabs Hitachi S-5500 instrument at different magnifications. Energy-dispersive X-ray spectroscopy (EDX) was performed to confirm PTA and IONPs in the STEM images.

3.7.5 *Vibrating sample magnetometer (VSM)*

The measurement of a sample's magnetic moment in a magnetic field serves as the foundation for VSM analysis. A magnetic field is applied to the sample, and the sample's magnetic moment is calculated as a function of the strength of the magnetic field. The magnetic moment of the sample is determined as a function of vibration frequency after it is subjected to mechanical vibration at a predetermined frequency. Important details regarding the sample's magnetic characteristics, such as magnetic anisotropy, magnetic domains, and magnetic susceptibility, can be learned from this measurement.



Figure 3-8: Vibrating sample magnetometer (VSM)

Small amounts of dry NPs were mounted on a sample holder in a Princeton PMC Model 3902 MicroMag, under a magnetic field of 10 kOe and the field increment was kept 100 Oe.

3.7.6 *Drop Shape Analyzer (DSA)*

The Drop Shape Analyzer DSA25 KRUSS was used to measure contact angle. The glass slide was prepared by dip coating in IONPs solution. A small water drop was placed on the surface of

the slide and the contact angle is then calculated based on the shape of the water droplet at the point of contact with the IONP coated slide. The DSA has a camera which continuously captures the image, and the software continuously processes the data and measures the contact angle. We could see the nature of the IONPs whether they are hydrophobic or hydrophilic with the help of continuous contact angle measurement.



Figure 3-9: Drop Shape Analyzer

3.7.7 X-Ray Crystallography (XRD)

Bruker D8 A25 DaVinci X-ray Diffraction (XRD) with $\text{CuK}\alpha$ radiation was used for XRD. LynxEye™ SuperSpeed Detector was used in examining the crystal structure of IONPs. X-Ray Diffraction, or XRD, is a method for examining the structure of crystalline materials. By exposing a sample to an X-ray beam, the atoms in the sample cause the X-rays to scatter in various directions. The arrangement of atoms in the material may be determined by measuring and analyzing the pattern of X-ray scattering. The voltage and current of X-ray source operate at 40Kv and 40mA respectively and the $\text{CuK}\alpha$ radiation have the wavelength of $\lambda = 1.5406 \text{ \AA}$. The XRD help in the identification of crystallinity and differentiate between crystalline and amorphous form.

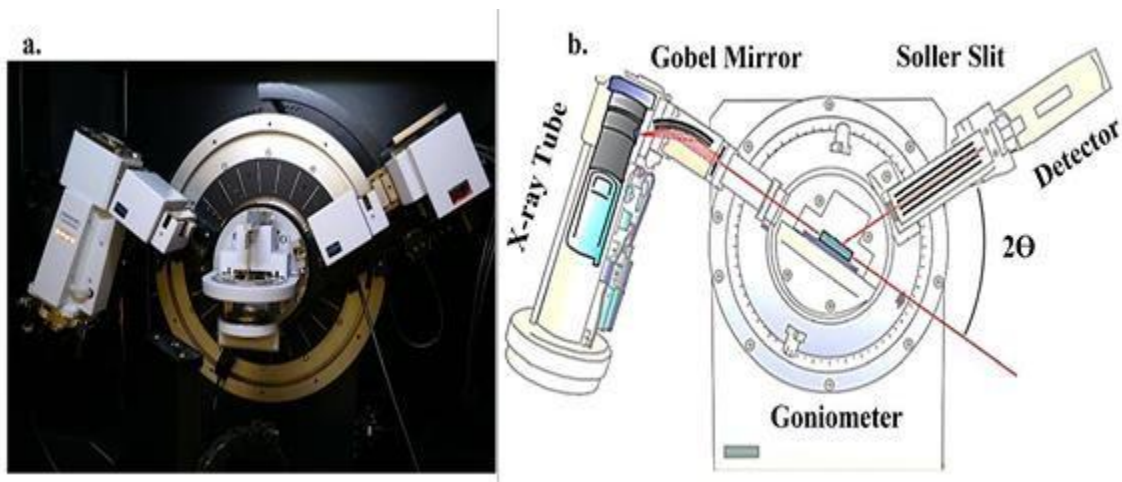


Figure 3-10: (a) Bruker D8 A25 DaVinci XRD (b) Schematic showing the main components of XRD

IONPs were placed and dried on silicon flats and analyzed. By exposing a sample to an X-ray beam(at instrument settings low_cryst,120min,10-75degrees,0.2degrees), the atoms in the sample cause the X-rays to scatter in various directions.

3.7.8 *Magnetherm*

NanoTherix MagneTherm NTNU-IKP1004 was used for nanoparticle hyperthermia testing and drug release characterization. By applying a magnetic field, the nanoTherics MagneTherm™ measures the specific absorption rate (SAR) of magnetic particles to determine their thermal absorption capacity. This instrument is also equipped with a UV-Vis spectrophotometer to obtain drug delivery release data, but only for magnetically responsive nanoparticles. The primary structure comprises a solenoid with nine or eighteen coils, linked to an electric current and a chiller to maintain a steady solenoid temperature. Additionally, a cap holding various-capacity capacitors (ranging from 6.2 to 200 nF) is present.

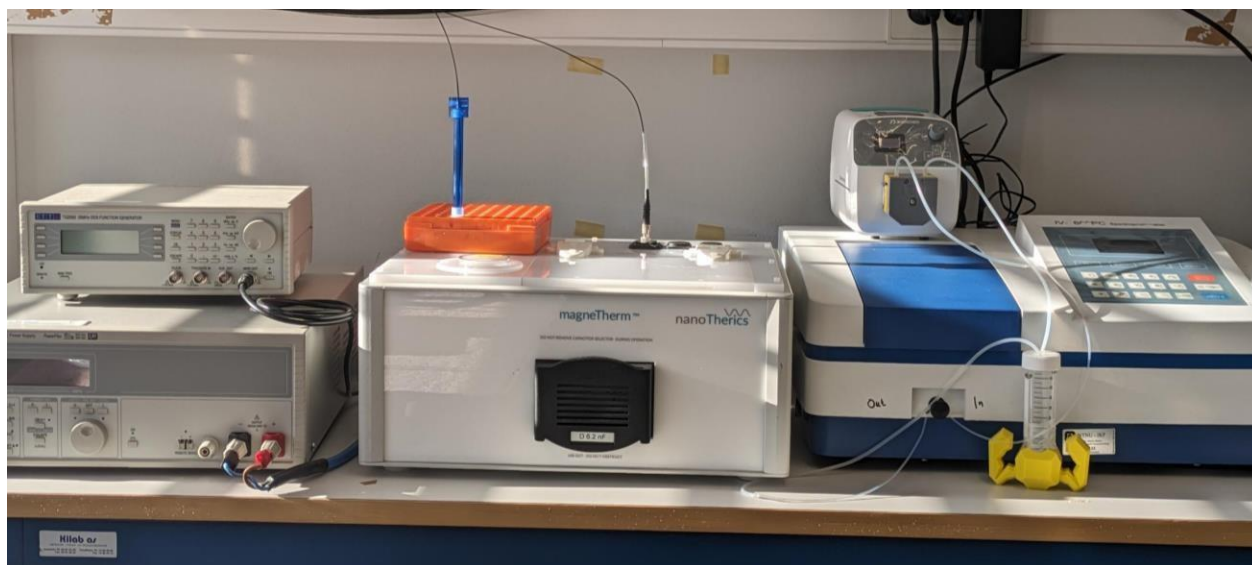


Figure 3-11: Nanotherics MagneThem

Nanoparticles were dispersed in 1 ml water for testing. Electromagnetic heating of nanoparticles was done to establish heating capacity over a range of frequencies to make response profiles. MagneTherm is attached to a UV-Vis Spectrophotometer which shows the absorbance for drug release under the applied magnetic field. Scan and OriginLab software were used for data .

3.7.9 Software:

All graphs and calculations of derivatives, mean values and standard derivations were done by the software Origin 2023 from OriginLab®. General schemes and graphical pictures were prepared with the help of BioRender® and ChemDraw®.

CHAPTER 4: RESULTS AND DISCUSSIONS

This chapter discusses the results of various experiments conducted in this project. The results are subjected to the objectives of the project and the objectives are a) Synthesis and characterization of hydrophobic Iron Oxide nanoparticles (IONPs) b) Encapsulations of IONPs and Paclitaxel in PLGA nanoparticles using flash nanoprecipitation c) Analyzing the SAR Values of IONPs and drug release in applied magnetic field using Magnetherm.

4.1 Synthesis of Iron oxide nanoparticles

Iron oxide nanoparticles were synthesized by two different methods and analyzed for their magnetic saturation and particle size. The method based on the purity of end product was used.

2..4.1 Method I:

4.2.1.1 XRD of Iron oxide nanoparticles

The XRD pattern Fig 4.1 d displays characteristic peaks corresponding to spinel iron oxide of magnetite. The 2θ values of 30° , 36° , 43° , 54° , 57° and 63° are attributed respectively to the planes (220), (311), (400), (422), (511) and (440). The broad peaks indicate the polycrystalline and ultrafine nature of the samples[93]. The crystal size derived from scherrer's equation comes out to be 10.89 nm.

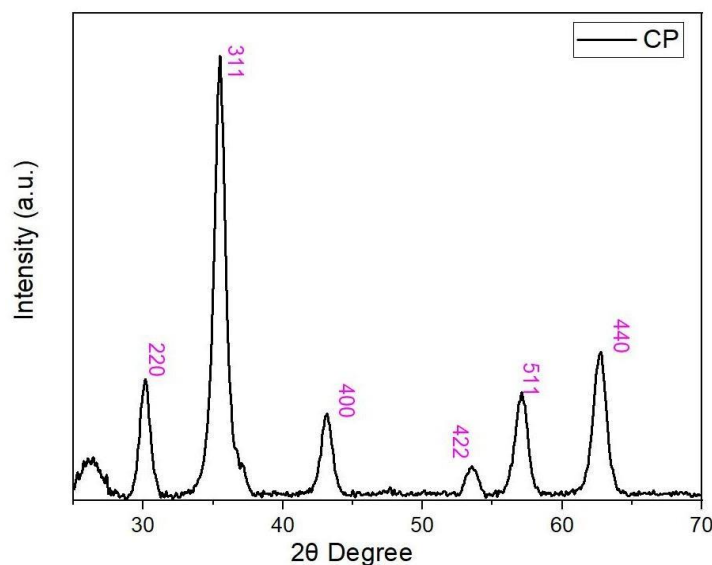


Figure 4-1: XRD pattern of IONPs

4.1.1.2 S(T)EM images of the Iron Oxide nanoparticles

The Iron oxide nanoparticles were imaged in BFSTEM mode in S(T)EM to see the morphology and size of the particles. Particles were at different instrument resolutions for better understanding of morphology. The particle size is between 7-30 nm. The exact morphology can not be determined from the S(T)EM images, but the particles appear to be spherical. These oleic acid particles appear to be less aggregated than the bare Iron oxide nanoparticles[93].

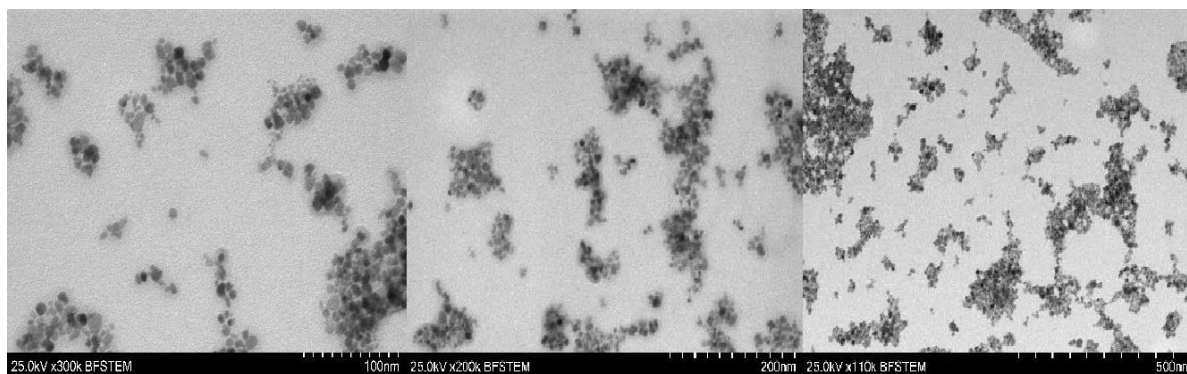


Figure 4-2 S(T)EM images of IONPs

4.1.1.3 VSM of the Iron Oxide nanoparticles

Since superparamagnetism is an important property of IONPs, VSM measurements were performed. The superparamagnetic characteristics of naked IONPs are shown in Fig., where remanent magnetization was not detected in the absence of a magnetic field. The saturation magnetization, M_s of NPs comes out to be 65.58 emu/g. Such values of saturation magnetization for IONPs have been reported in the literature [96]

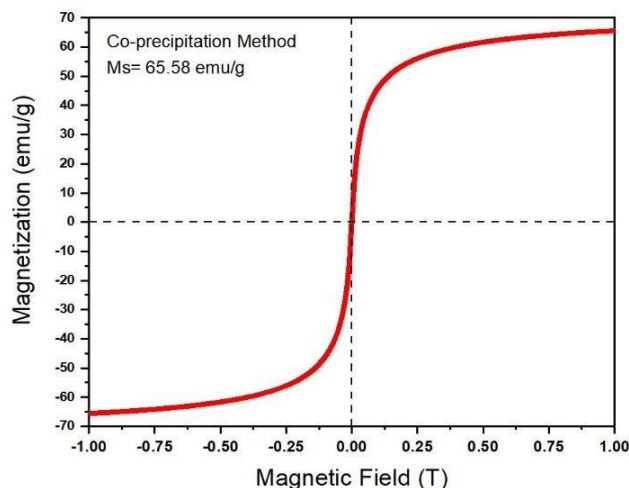


Figure 4-3 VSM of IONPs

Although the Iron Oxide nanoparticles synthesized by this method had the required characteristics but there were some challenges in the washing of these nanoparticles. The particles were not separating well on the magnet. As these nanoparticles were to be used in the flash nanoprecipitation the washing of the excess oleic acid and other impurities is important.

Another method was tried which is attributed as method II in this thesis.

4.1.2 Method II.

4.1.2.1 XRD of bare and oleic acid coated Iron oxide nanoparticles

The XRD pattern Fig 1 d displays characteristic peaks corresponding to spinel iron oxide of magnetite. The 2θ values of 30° , 36° , 43° , 54° , 57° and 63° are attributed respectively to the planes (220), (311), (400), (422), (511) and (440). The pattern of Oleic acid coated IONPs shows a decrease in the intensity resulting in broadening of the peak due to the coating of oleic acid [96, 97]. The crystal size derived from Scherrer equation was 9.68 nm for bare IONPs and 8.76 for the oleic acid coated IONPs which align with their S(T)EM sizes.

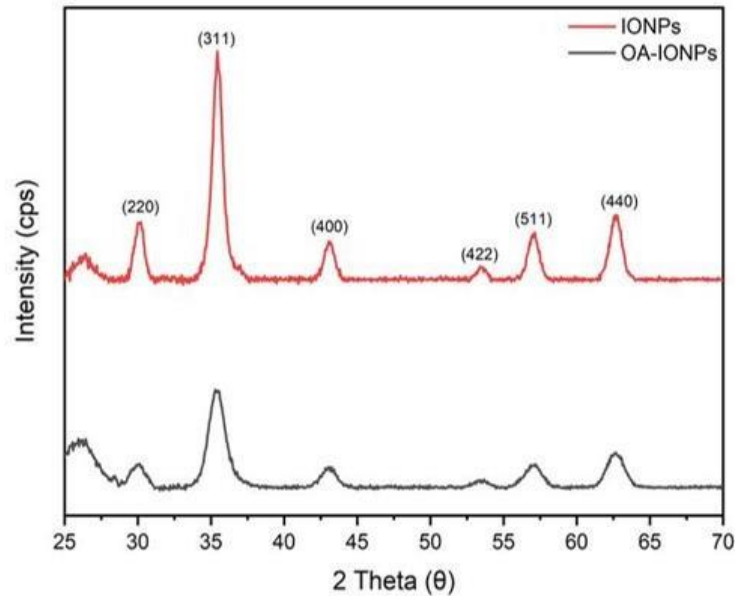


Figure 4-4 XRD of bare and oleic acid coated IONPs

4.1.2.2 TEM images and DLS of the bare and oleic acid coated Iron Oxide nanoparticles

Though, the average hydrodynamic diameter of IONPs nanoparticles was found to be 139 nm from DLS, but S(T)EM image indicated the particle size in the range of 10–30 nm. A particle's diameter that includes this hydrated electrical layer is referred to as its hydrodynamic diameter. Consequently, it is anticipated that the hydrodynamic diameters will be larger than the diameters determined from bright field TEM images, which show the particles as dry. It was found that the measured hydrodynamic diameters were roughly five to ten times greater than an individual IONP's dry diameter. For Fe₃O₄ -OA particles the average hydrodynamic diameter of nanoparticles was 57 nm, and the S(T)EM images indicated the particle size again in the range of 7-30 nm fig 1 c. Although, for Fe₃O₄ -OA the hydrodynamic dia was measured in organic solvent i.e., THF, but the decrease in size could also be due to less aggregation of nanoparticles because of oleic acid coating, which can also be seen in the S(T)EM image below.

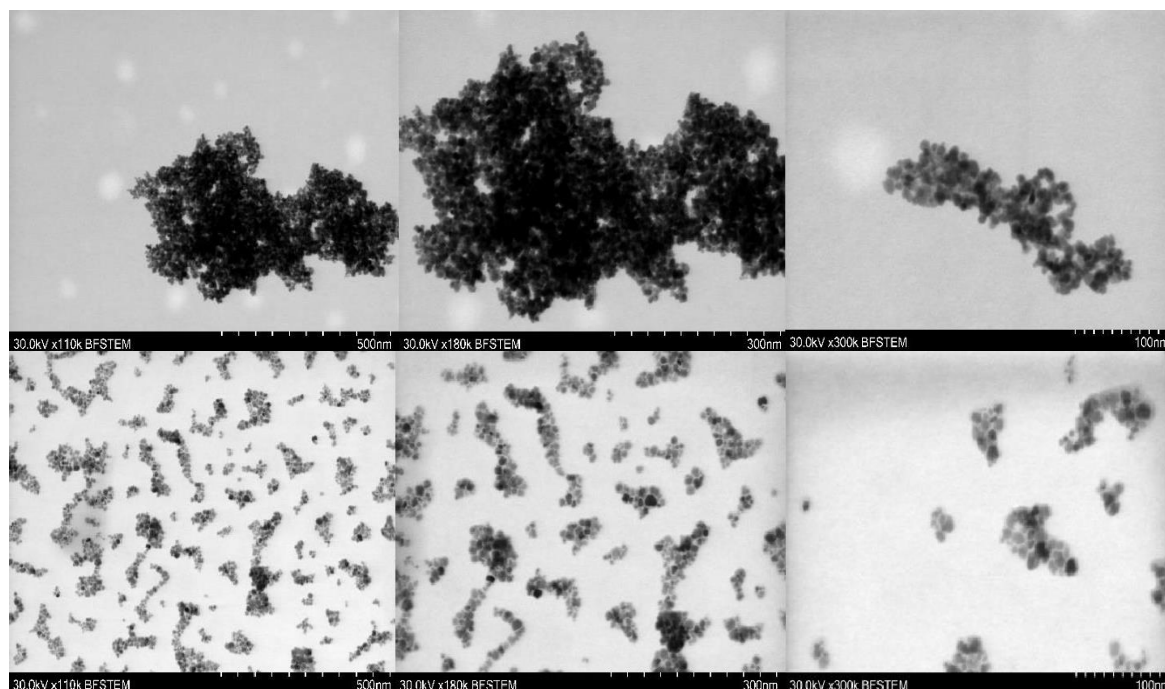


Figure 4-5 S(T)EM of bare and oleic acid coated IONPs

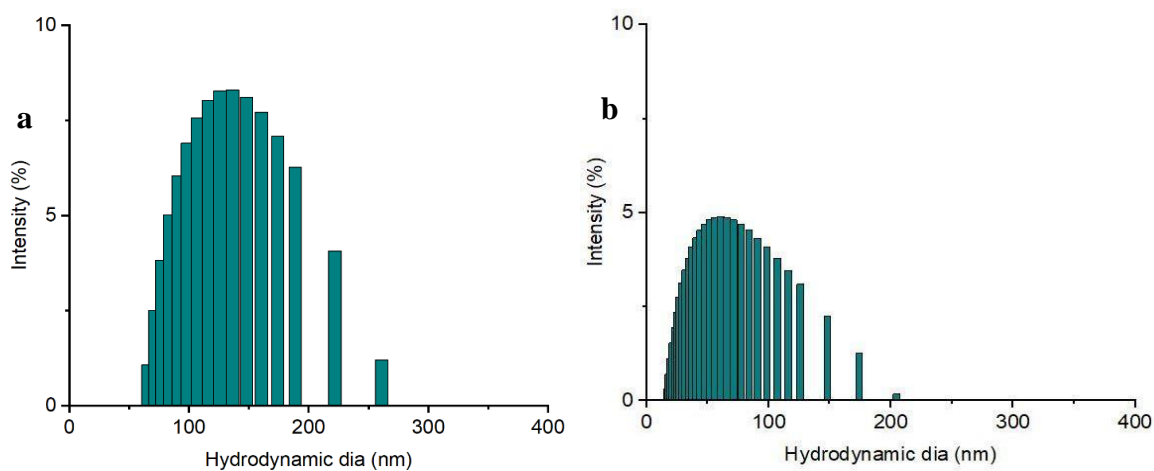


Figure 4-6 Hydrodynamic dia of (a) bare and (b) oleic acid coated IONPs

4.1.2.3 VSM of bare and oleic acid coated Iron Oxide nanoparticles

VSM measurements were performed to understand the magnetic properties of bare IONPs and OA-IONPs (Figure 4.7). In both cases, no remanent magnetization was observed in the absence of a magnetic field, a characteristic typical of superparamagnetic materials. The saturation magnetization, M_s of NPs was decreased from 64 emu/g to 62 emu/g after the coating of oleic acid. According to a publication [98], there was a decrease in the

saturation magnetization of nanoparticles when the resulting particle size decreased. Indeed, the surfaces of magnetic nanoparticles (MNPs) have a disordered spin layer, and as the particle size drops, the disordered layer to MNP radius ratio becomes substantial. For smaller nanoparticles, surface spin disorder consequently results in a lower M_s value. Lower M_s values may potentially be related to the presence of a diamagnetic shell that encased the NPs[99]. In this instance, the OA coating layer may have prevented the oxidation reaction that would have otherwise decreased the magnetic dipole–dipole interaction between the NPs samples.[96, 100].

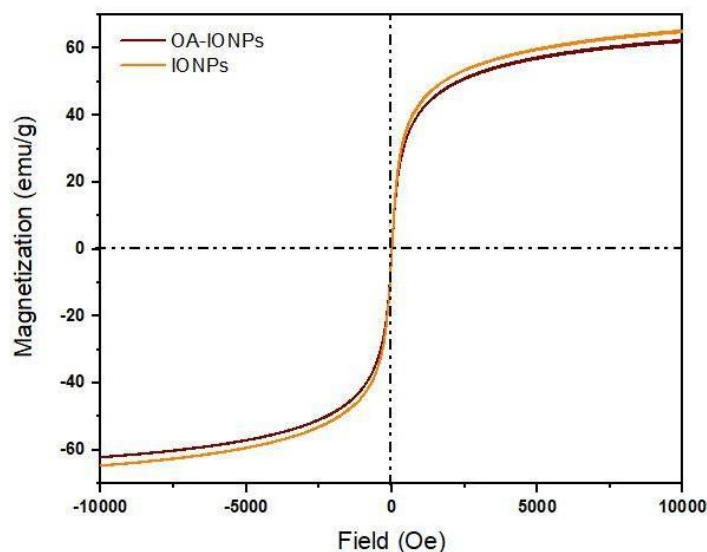


Figure 4-7 VSM of bare and oleic acid coated IONPs

4.1.2.4 FTIR of Oleic acid, bare IONPs and Oleic acid coated IONPs

Using FTIR spectra analysis, the surface coating of IONPs with oleic acid was investigated further and contrasted with IONPs that were bare and with pure oleic acid (Fig. 2). The recognizable peaks were detected at approximately 2920 and 2850 cm^{-1} for both symmetric and asymmetric $-\text{CH}_2$ stretching in oleic acid and oleic acid coated IONPs. The presence of oleic acid coating on iron oxide nanoparticles was indicated by the absence of similar peaks in the uncoated nanoparticles. There was no discernible $-\text{OH}$ stretching peak for pure oleic acid because it overlapped with the $-\text{CH}_2$ stretching [101]. Nonetheless, a noticeable peak at 932 cm^{-1} indicates the bending (out of plane) of the carboxylic acid $-\text{OH}$ bond. Furthermore, because of the anchoring on the nanoparticle surface, the carboxylic $\text{C}=\text{O}$ stretching seen in oleic acid, which is reflected by the steep peak at 1709 cm^{-1} , is absent from OA-IONPs.

[102]. The -COOH anchoring on the surface of the nanoparticles is the cause of the aforementioned carboxylic stretching disappearing in OA-IONPs. Additionally, the -OH peak absence occurs at 1516 and 1411 cm^{-1} , which is ascribed to the carboxylate (-COO-) stretching, signifying ligand binding on the surface of the nanoparticle [103]. The peaks located at lower wavenumbers of 554 cm^{-1} indicate the presence of Fe-O stretching in magnetic nanoparticles that are coated with oleic acid and those that are not.

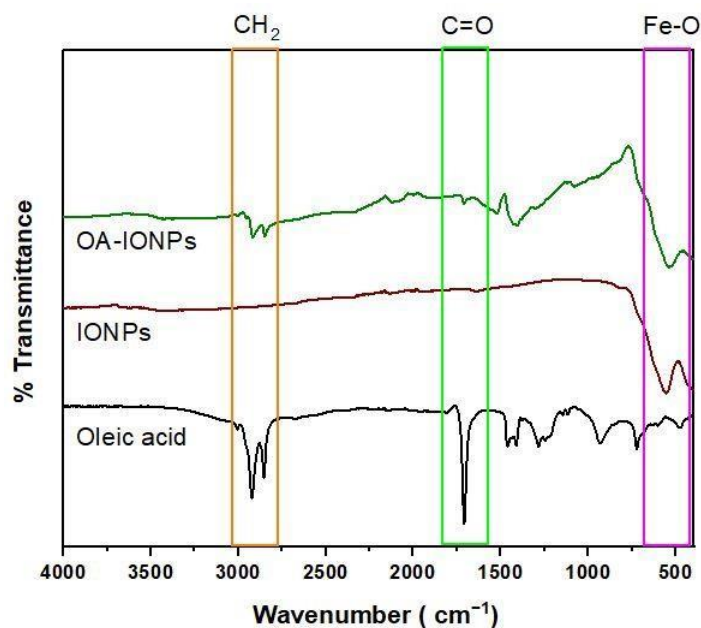


Figure 4-8 FTIR of oleic acid, bare IONPs and oleic acid coated IONPs

4.1.2.5 Contact angle of bare and Oleic acid coated particles

As discussed earlier, the purpose of oleic acid coating on Iron oxide particles is to make them hydrophobic to later use them in flash nanoprecipitation, to confirm the hydrophobicity of the coated nanoparticles, their contact angle was measured.

Fig a represents the contact angle of bare Iron oxide nanoparticles while Fig b represents the contact angle of oleic acid coated iron oxide nanoparticles. The increase in contact angle from 9.7° to 94.5° confirms the hydrophobic nature of the coated iron oxide nanoparticles.

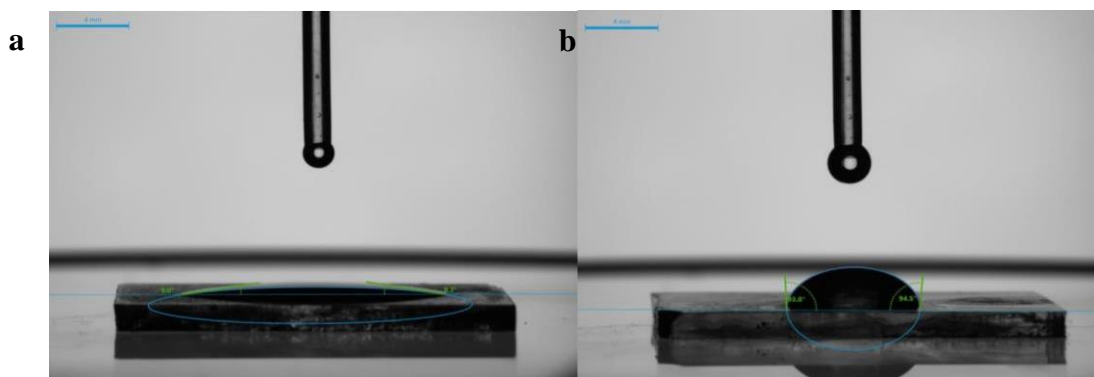


Figure 4-9 Contact angle of (a) bare IONPs and (b) oleic acid coated IONPs

4.1.2.6 Optimization with different Oleic acid volumes

From the DLS of bare and oleic acid coated IONPs it was clear that the hydrodynamic size was decreasing after coating of oleic acid. From the STEM images it was evident that it could be due to less aggregation of particles. So, the process was optimized to get the minimum hydrodynamic size of the nanoparticles. For 0 ml of the oleic acid the hydrodynamic size was measured in water while the other samples were measured in THF. For 1.2 ml of the oleic acid the hydrodynamic size was minimum i.e., 57 ± 0.27 nm. It can be said that, size of IONP was dependent on the loading of oleic acid. The decrease in size could be due to less aggregation of nanoparticles because of oleic acid coating, which can also be seen in the S(T)EM image. The reason for the larger hydrodynamic size of IONPs in the case of lower oleic acid volumes was that there was not enough oleic acid to encapsulate IONP, which made it harder for IONP to separate during ultra-sonication. Larger hydrodynamic size IONPs are thus formed as a result.

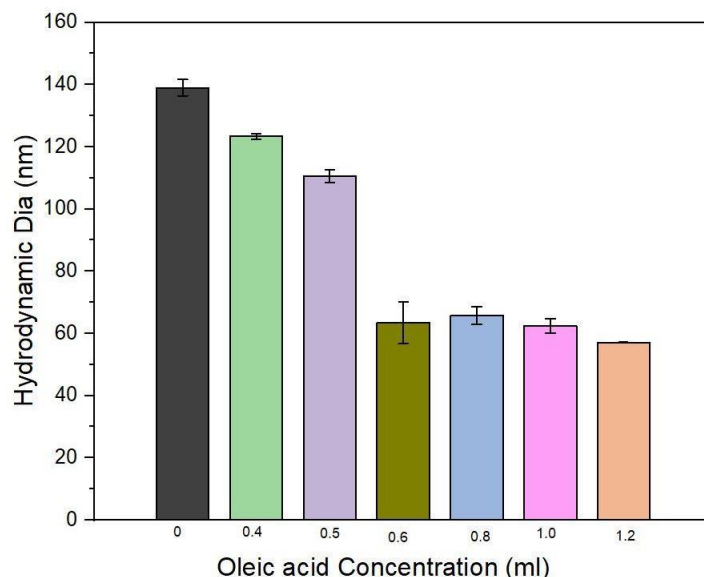


Figure 4-10 Optimization of particle size with increasing oleic acid volumes

These optimized OA-IONPs were encapsulated in PLGA by flash nanoprecipitation. Before encapsulation bare PLGA nanoparticles were made by FNP and process conditions were optimized for encapsulation of IONPs in PLGA.

4.2 Synthesis of bare PLGA nanoparticles

Bare PLGA nanoparticles were synthesized by FNP and following characterizations were performed to know the size and morphology of the particles.

4.2.1 STEM images and hydrodynamic dia of bare PLGA nanoparticles

The images shown below are for 2 wt.% of PLGA. The particles were stained with phosphotungstic acid for better contrast in STEM. Looking at their morphology in STEM, the particles appear to be spherical. An organic solvent that is water miscible dissolves the polymer. Supersaturation is caused by the fast (and turbulent) mixing of the organic solvent stream with water, which starts the precipitation of the dissolved hydrophobic components.

We assume the particles are making spaghetti like structures with more hydrophobic parts of the PLGA towards the center and relatively less hydrophobic parts forming a shell. The basic principle of particle formation is similar to one explained by Kevin. M et al [74]. Based on our own hypothesis we assume the particles are making spaghetti like structures with more hydrophobic parts of the PLGA towards the center and relatively less hydrophobic parts forming a shell. The

STEM size of the 70 particles counted comes out to be $140\text{nm}\pm 10$ while the hydrodynamic dia is 195 ± 4 nm.

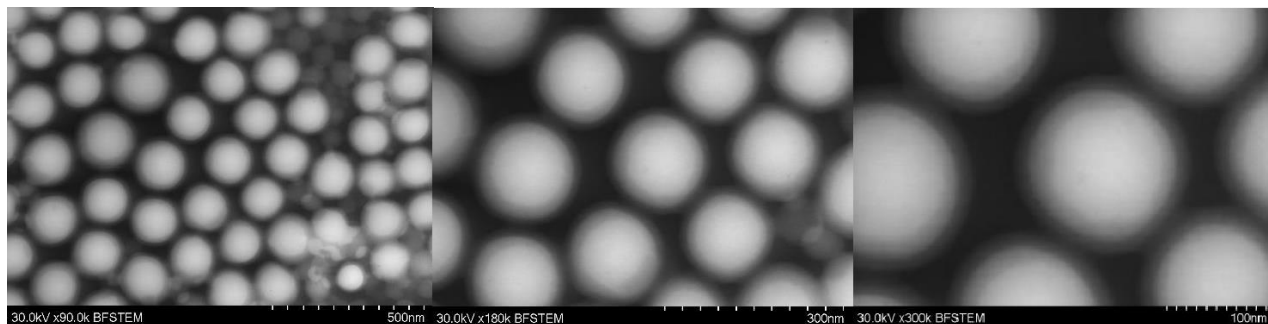


Figure 4-11 S(T)EM images of bare polymeric particles

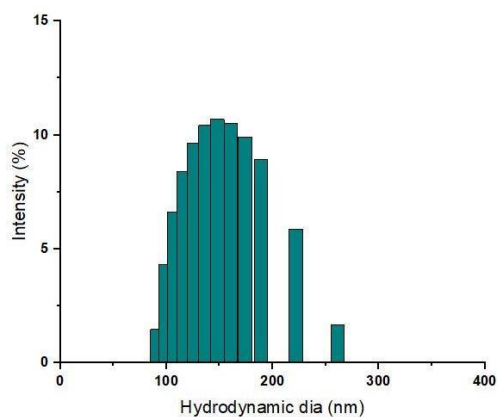


Figure 4-12 Hydrodynamic dia of bare polymeric particles

4.2.2 Optimization with different PLGA weight %

As we had to use these polymeric nanoparticles to encapsulate IONPs and paclitaxel and later use for biomedical applications the size of these particles is of critical importance. Previously it has been observed that particle size is a function of polymer weight%.[104] The hydrodynamic dia came out to be 161 ± 3.8 nm, 182 ± 6 nm and 195 ± 4 nm for PLGA 1 wt% ,1.5 wt% and 2 wt% respectively. The error bars indicate standard deviations of three measurements of DLS for the same sample. So, particles with weight% 1 were explored further in the thesis. So that even after encapsulation of IONPs the particle hydrodynamic is in the range i.e, 200 nm to be used for biomedical applications.

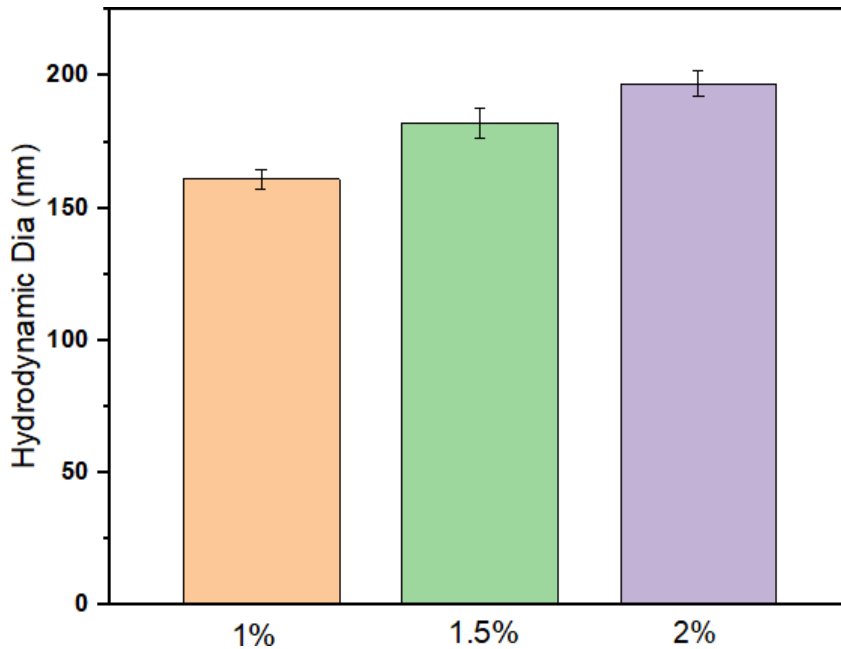


Figure 4-13 Optimization of particle size with increasing PLGA wt%

4.3 Synthesis of PLGA coated Iron Oxide nanoparticles

4.3.1 S(T)EM images and Hydrodynamic dia of PNPs@IONPs

For these particles 1 wt% PLGA and 1mg/ml of IONPs were used. From the STEM images we can see the encapsulation of IONPs in polymeric nanoparticles. The organic solutes (i.e., IONPs) and polymer are dissolved in a water miscible organic solvent. Rapid (and turbulent) mixing of the organic solvent stream with water induces supersaturation, which initiates precipitation of the dissolved hydrophobic components. Prud'homme et al. [105] proposed that the hydrophobic end of the polymer and the hydrophobic solutes are encapsulated in the core of the nanoparticle. The hydrophilic end of polymer forms a corona, sterically stabilizing the particles by preventing further aggregation. For the successful encapsulation of the IONPs it is important that nucleation and growth time for polymer and hydrophobic IONPs should be same. The hydrodynamic dia of these particles is 177 ± 3 nm which is greater than that for bare PNPs at 1 wt%. The increase in hydrodynamic size could be encapsulation of IONPs in the PNPs or due to aggregation because these nanoparticles are centrifuged for washing purposes.

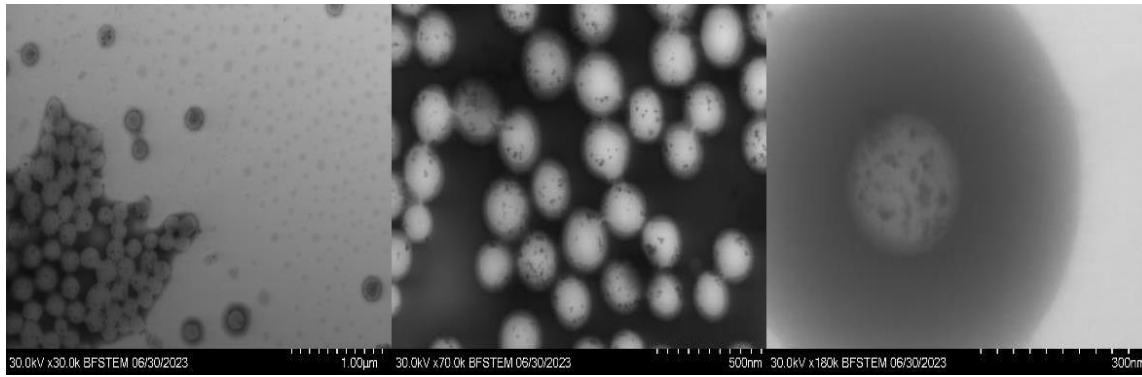


Figure 4-14 S(T)EM images of Polymer encapsulated IONPs

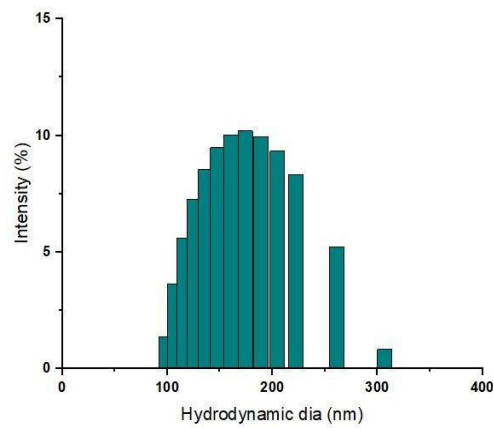


Figure 4-15 Hydrodynamic dia of Polymer encapsulated IONPs

4.3.2 Energy Dispersive Spectroscopy (EDS) of particles

EDS was done for qualitative analysis of the samples. Image on the right provides the elemental analysis of the image on the left. The constituents elements of PLGA are C, H and O, while that of IONPs are Fe and O. The staining agent contains P, W, H and O. Hydrogen can not be detected through EDS. The grid is carbon coated and explains the abundance of carbon in analysis. But we can see a rise in carbon peak along with other peaks at the sample sites.

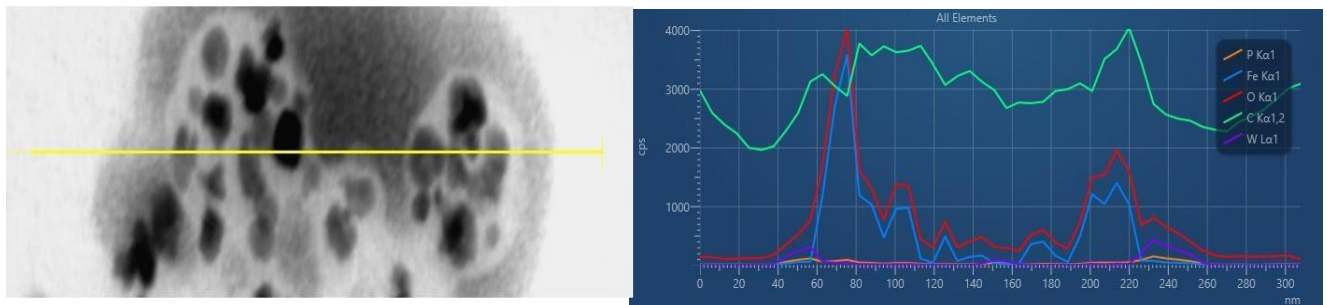


Figure 4-16 EDS of Polymer encapsulated IONPs

4.3.3 Optimization with different IONPs concentrations

For the rest of study it is important to have more Fe content in the core of polymer encapsulated IONPs so the concentration of ionps was increased from 1mg/ml to 6 mg/ml for sample a to f shown in Fig 4.17. As the concentration of hydrophobic IONPs increases their supersaturation increases and they precipitate faster than the polymeric particles and come out on the surface PNPs as can be seen in fig d,e and f. For 3mg/ml IONPs concentration we can see more particles encapsulated and continued the rest of studies with this concentration.

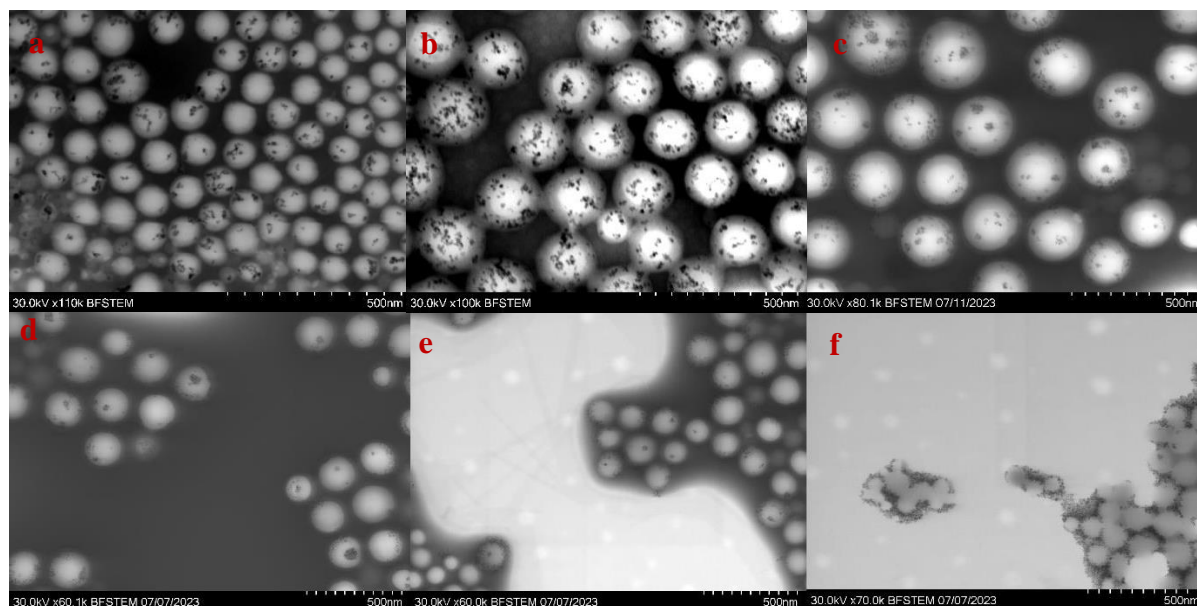


Figure 4-17 S(T)EM images for increasing concentration of IONPs in polymer encapsulated IONPs

4.3.4 FTIR of OA-IONPs, PNPs and PNPs@IONPs

The surface chemistry of bare polymeric particles and polymer encapsulated IONPs was studied and compared by FTIR spectra analysis Fig 2. the peaks at the lower wavenumbers 554 cm^{-1} represent the Fe–O stretching in both OA-IONPs, and polymer encapsulated IONPs. A strong peak corresponding to carbonyl stretching was observed near 1720 cm^{-1} in both bare polymeric particles and polymer encapsulated IONPs, which cannot be seen in OA-IONPs justifying the existence of PLGA.

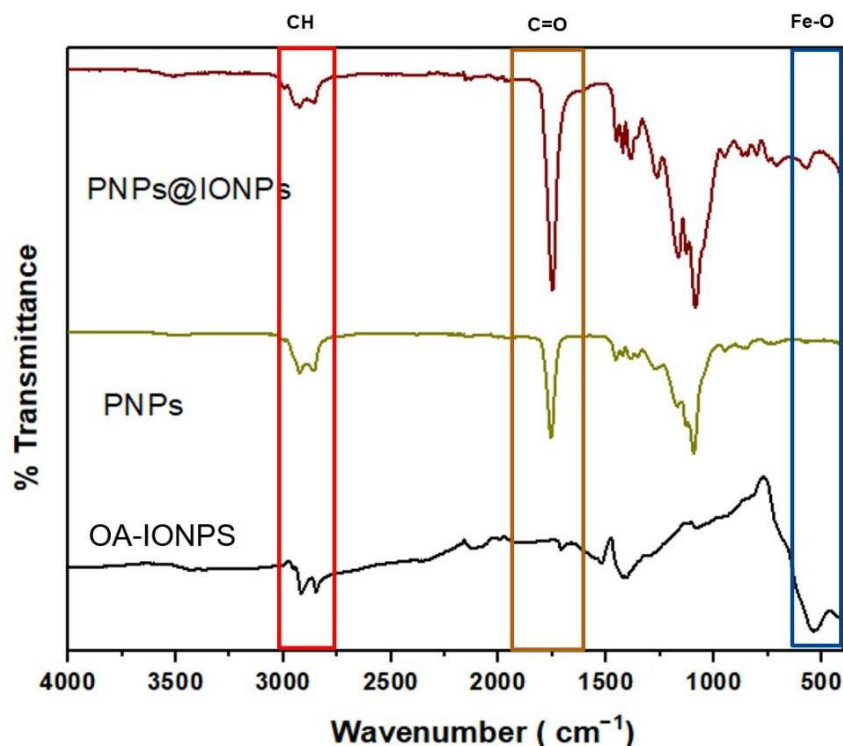


Figure 4-18 FTIR of OA-IONPs, PNPS and PNPs@IONPs

4.3.5 TGA of OA-IONPs, PNPS and PNPs@IONPs

For the quantification of IONPs in Polymer encapsulated IONPs thermogravimetric analysis was done. According to the results, PNPs and PNPs@IONPs exhibited the onset of decomposition at a temperature lower than that observed for the uncoated IONPs, which arises from the presence of the polymer and polymer coating, respectively. 33.35% mass loss was observed around 350°C for PNPs @IONPs. From 400°C to 500°C the mass loss was 58.11%. And the lastly the mass loss from 500°C to 700°C was 10.56% . While for bare IONPs there was about 4% mass loss till 500°C and after that it became constant. For OA-IONPs the mass loss comes out be 60% confirming the remaining 40% to be Fe compound content which comes out to be equal to theoretical amount put in.

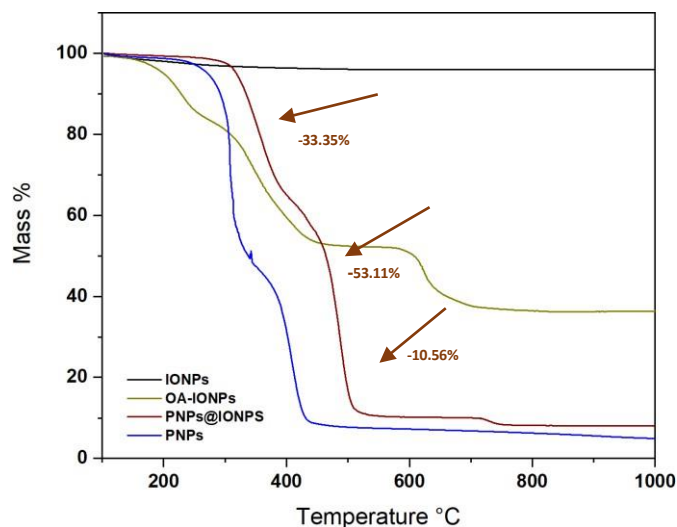


Figure 4-19: TGA of IONPs,OA-IONPs, PNPs and PNP@IONPs

4.3.6 VSM of PNP@IONPs

The magnetization curves of polymer-encapsulated IONPs at room temperature displayed zero coercivity and no remanence, which are hallmarks of superparamagnetic behavior. But the drop in Magnetic saturation value is huge. The decrease in M_s value could be due to diamagnetic behavior of PLGA coating layer. Although the M_s values is much lower as compared to bare IONPs, but these particles can still be pursued for drug release in applied magnetics with the M_s value of 42 emu/g.

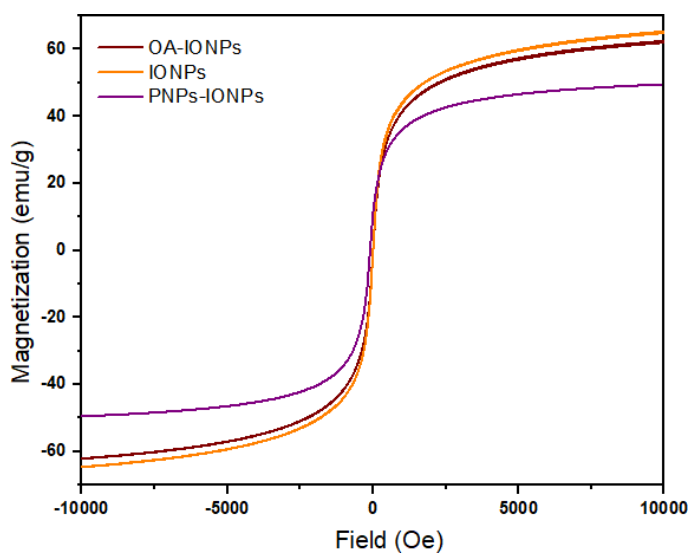


Figure 4-20 VSM of IONPs , OA-IONPs and PNP@IONPs

4.4 Hyperthermia and Drug release

This section explains the analytical techniques used to observe the release of the drug in order to verify the controlled drug release. In the nanoTherics magneTherm setup we can measure the SAR values and drug release separately as well as in combination. The setup was first optimized for the maximum Specific absorption ratio (SAR) with different combinations of applied magnetic field and frequency. Then for the optimized combination drug release studies were performed. Further discussion about SAR and drug release can be found in the following sections.

4.4.1 Hyperthermia and SAR Values

As discussed in the literature and theory chapter, the specific absorption rate (SAR) is commonly used to quantify the heating efficiency of magnetic colloids. For this thesis the SAR values were calculated using the Nanotherics MagneTherm.

In the figures **4.21 (a) and (b)** the capacitors associated with certain frequency are mentioned. The magnetic field was applied at different frequencies i.e, 162.2kHz, 243.5kHz and 930.7kHz for 9 turns coil and 102.5kHz, 154.0kHz and 587.5kHz for 18 turns coil respectively. The frequencies were fixed and applied magnetic field was varied to perform the hyperthermia studies at Brezovich limit and 5 times of the Brezovich Limit as shown in **Fig 4.21**. The Brezovich criterion, $H_0 f \leq 485 \text{ MA m}^{-1} \text{ s}^{-1}$, was experimentally determined to be a physiologically tolerable level of prolonged exposure (more than 1 h) to the torso.[106]Where H_0 is the applied magnetic field and f is the frequency.

As shown in **Fig 4.21 a** there is no significant difference in the SAR values for different combinations of frequency and applied magnetic field at the Brezovich limit but at 5X brezovich the SAR vale increases 5-7 times except for 930.7kHz where it increases about 33 times. **Fig 4.21 b**. The maximum SAR value comes out to be 88.01 W/g for 102.fkHz and 30mT applied magnetic field. This combination was chosen for further optimization.

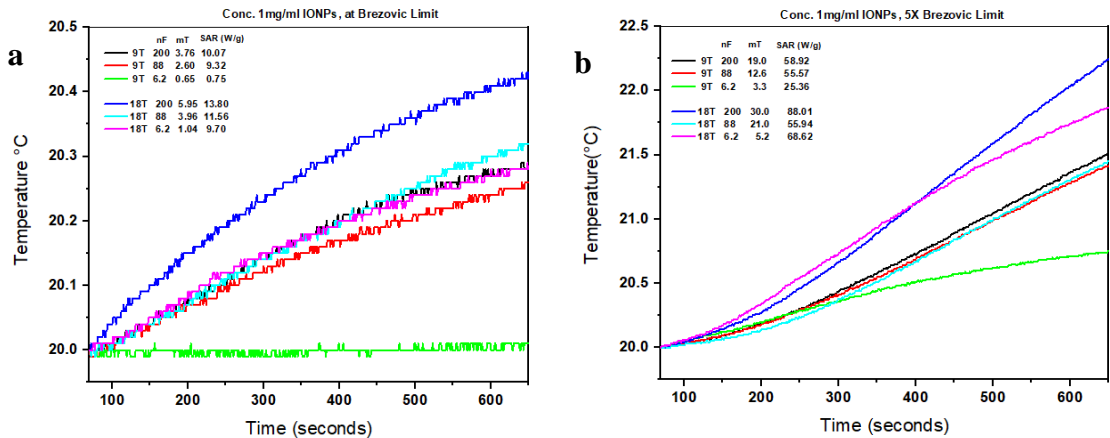


Figure 4-21 (a) Optimization for maximum SAR value at 1mg/ml at Brozovich limit (b) Optimization for maximum SAR value at 1mg/ml at 5X Brezovich limit

With increasing concentrations of IONPs from 1mg/ml to 3mg/ml although there is an increase in slope $\frac{\Delta T}{\Delta t}$ but the SAR value came out to be lower, which could be possible due to the inverse relation between SAR and mass of iron oxide nanoparticles. While for the fixed 3mg/ml concentrations we can see substantial increase in both the $\frac{\Delta T}{\Delta t}$ and SAR values at 10X times of the Brezovich limit **Fig 4.22**. SAR values as a function of concentration has been reported many times in the literature. [107, 108]

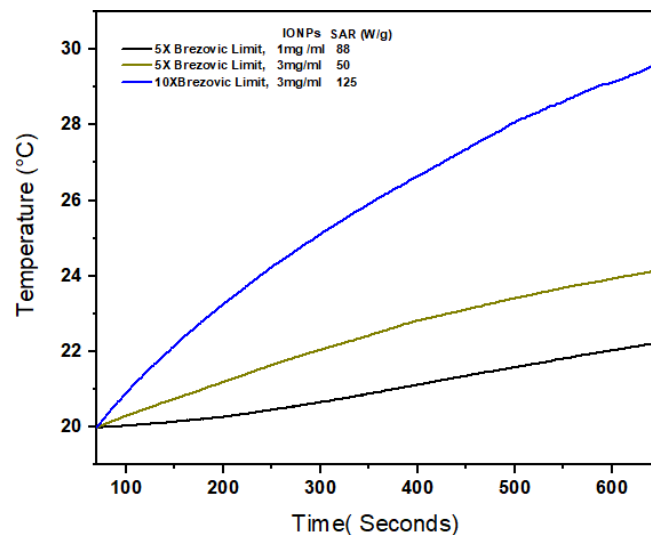


Figure 4-22 SAR values at different concentrations of IONPs

As per TGA results the total Fe compound content in the PNP@IONPs is 9.7%, it means that 3mg/ml of the PNP@IONPs will contain only 0.29 mg/ml of the Fe content. Since the increase

in temperature in MagneTherm is associated with the magnetic moment of IONPs the decrease in temperature difference in the figure below is justified due to less Fe content in PNP@IONPs as compared to bare IONPs.

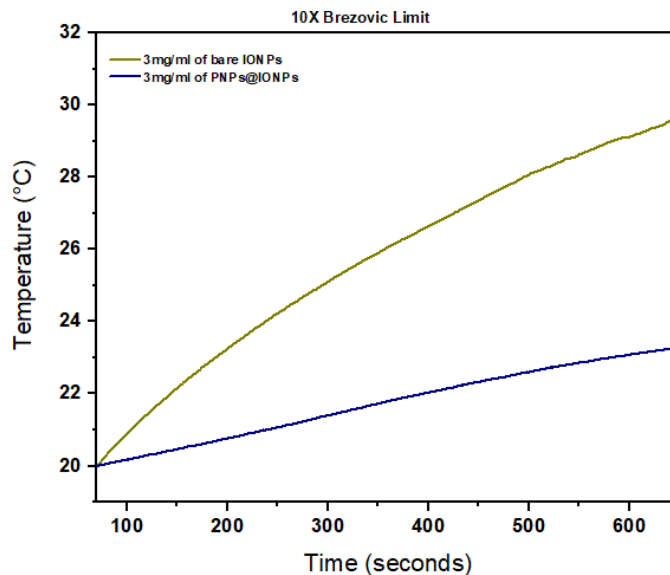


Figure 4-23: SAR values of bare IONPs and PNP@IONPs

4.4.2 Drug release

4.4.2.1 Calibration Curve

The calibration curve is a fundamental step to estimate the amount of released drug, comparing the unknown values with the calibration data. To establish the calibration curve for our system, paclitaxel was run in the Flash nanoprecipitation setup under the same condition as for co-encapsulation of drug and IONPs to get the concentration in total solution. Even though we are washing the samples after FNP it will contain some amounts of THF as its water miscible and Tween 80. That's why the FNP system was chosen to draw the calibration curve. The solution consisted of THF and water containing 0.1 W/V % of T80 in the same ratios as for encapsulation of drug and IONPs. **Fig.4.24** shows the absorbance peaks for different samples concentrations.

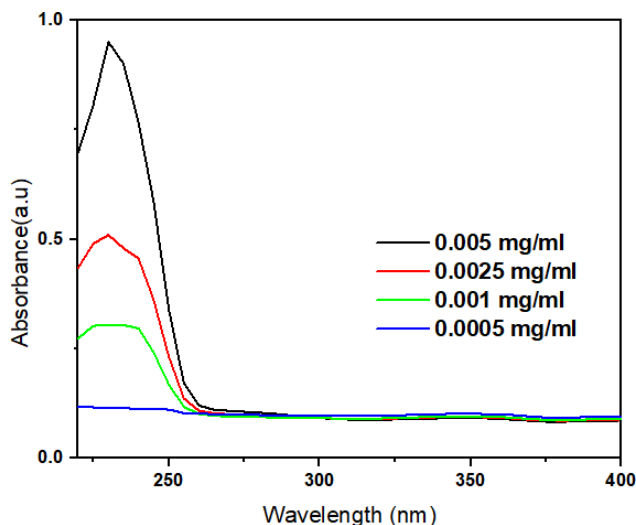


Figure 4-24 Absorbance peaks for Paclitaxel at different concentrations(mg/ml)

With the obtained data from UV-Vis the calibration curve is obtained by plotting absorbance values at 230 nm versus concentrations of the samples. The value of R^2 is equal to 0.9896. This curve was further used to compare the drug release from the system.

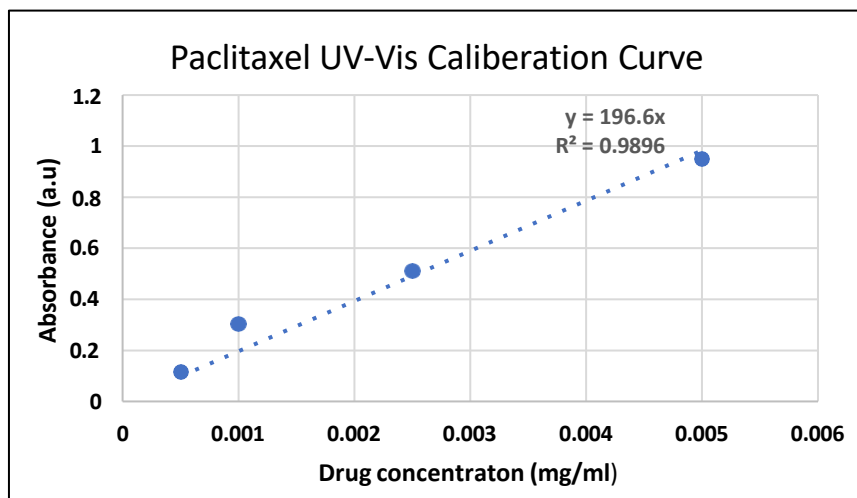


Figure 4-25 Paclitaxel UV-Vis calibration curve with the Lambert-Beer law

4.4.2.2 Drug Release in the applied magnetic field

First the drug release in magneTherm was done in the absence of magnetic field **Fig 4.26 (a)**. The sample was placed in a dialysis membrane with molecular weight cut off between 8-10KDa (smaller than NPs but greater than Paclitaxel). At room temperature i.e., 22.5°C, the dialysis membrane was placed in water. It was hypothesized that the drug will diffuse through membrane

towards water solely because of concentration gradient. Continuous readings were noted for the water with UV-Vis equipment attached with magneTherm but no magnetic field or temperature controls were turned on. After 50 mins there was not substantial drug release.

The same study was repeated this time with the applied magnetic field turned on (102.5kHz, 30mT). And the chiller temperature was set at 25°C. We can see an increase in temperature with the applied magnetic field Fig 4.26 (b), and with the increase in temperature we can see the increase in absorbance in UV-Vis. The increase in absorbance confirms the drug release during the process. The PLGA is not reported to be temperature sensitive polymer, so we conclude that the drug release is because of diffusion aided by increase in temperature.

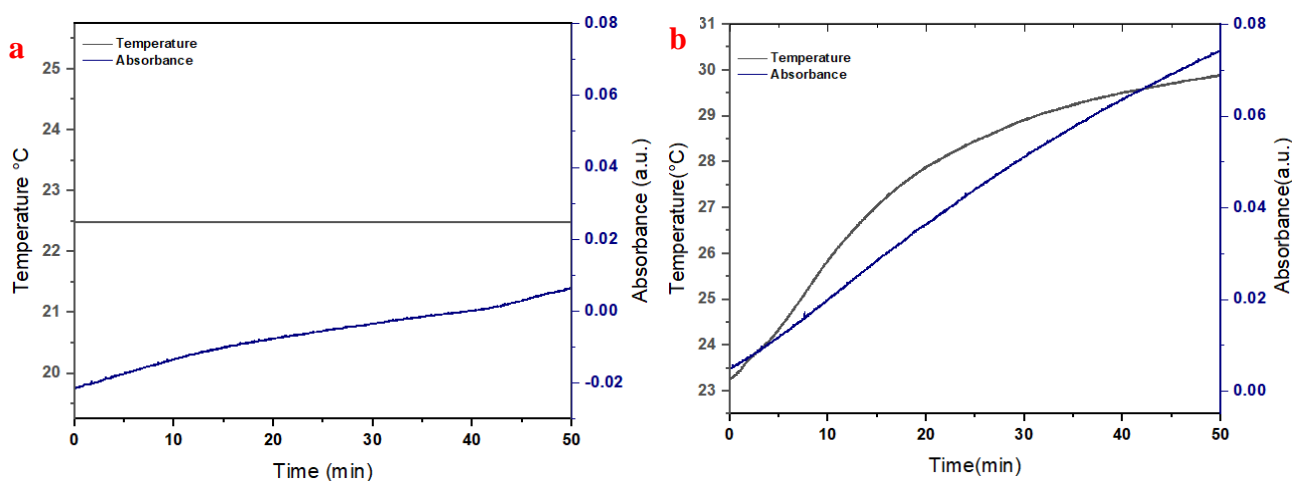


Figure 4-26 (a) drug release in absence of magnetic field (b) drug release in applied magnetic field

Further studies were done with pulse magnetic fields to make an optimized controlled drug release system. For the first study pulsed magnetic field was applied such that the magnetic field was applied for four exposures of 15 minutes while the time between each exposure was also kept 15 minutes. In the graph below the textured areas are the one where applied magnetic field is turned on. The flattening of curve can be observed when the magnetic field is turned off and temperature starts to decrease after each exposure as shown in Fig 4.27. If we compare the absorbance for which is a measure of drug release for Fig 4.26 b and Fig 4.27 at 50 mins we can see a decrease in the value. Which suggests that one can control the drug dosage magnetically over periods of time.

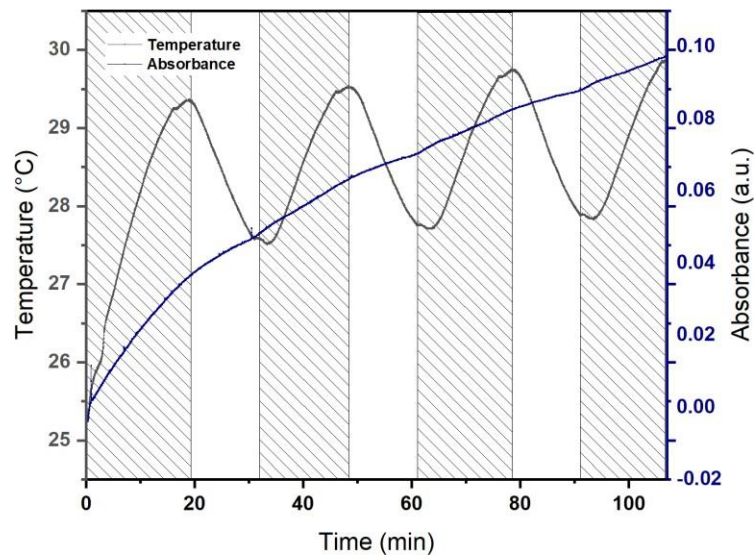


Figure 4-27: Controlled drug release in pulsed magnetic field, textured area represents when the magnetic field is turned on

From the results in **Fig 4.27** it was assumed that the sample needs more time to come to its original temperature and in turn minimize the drug release when the applied magnetic field is turned off. So the system parameters were varied such that the magnetic field was applied for three exposures of 15 minutes while the time between each exposure was kept 30 minutes. The flattening of the curve in the absence of magnetic field is more evident in this case as shown in **4.28**. And at 50 mins the value of absorbance is much lower than that in Fig 4.26 b.

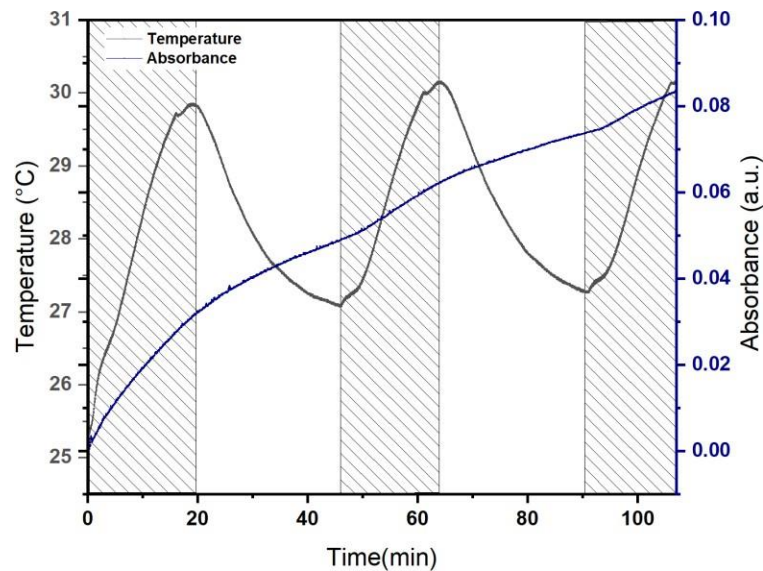


Figure 4-28 Controlled drug release in pulsed magnetic field, textured area represents when the magnetic field is turned on

The hypothesis was tested for another set of parameters. Two exposures of 45 mins were set where the time between exposures was also set for 45 minutes. We observe the variations in curves with applied magnetic field. The sudden increase in release at 20 mins could be due to a sudden external force on the membrane which resulted in shaking of and release from the surface of membrane.

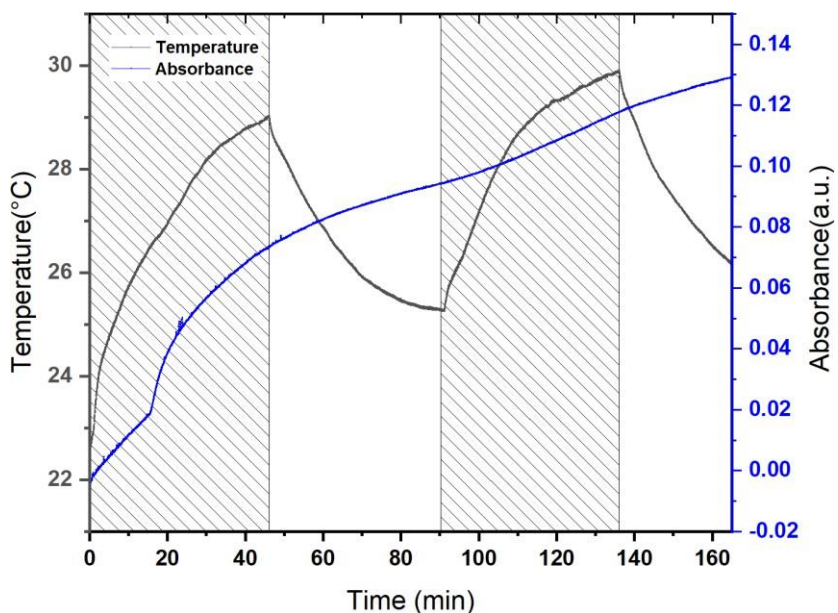


Figure 4-29: Controlled drug release in pulsed magnetic field, textured area represents when the magnetic field is turned on

Next, the drug release was observed first with applied magnetic field for 1 hour and then without the magnetic field. One can clearly see the change in release profile when the applied magnetic field is turned off as shown in **Fig 4.29**

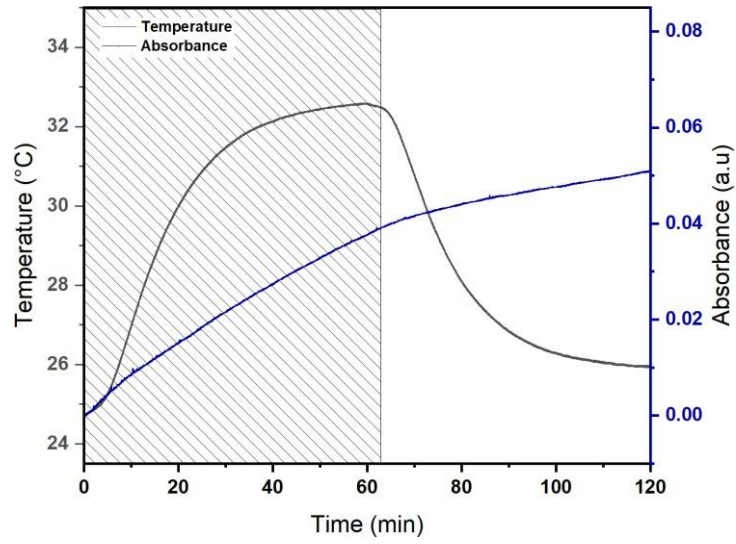


Figure 4-30: Controlled drug release in pulsed magnetic field, textured area represents when the magnetic field is turned on

From the results discussed above, it is concluded that one can co-encapsulate magnetic iron oxide nanoparticles and paclitaxel in PLGA using flash nanoprecipitation. And later use for magnetically controlled drug release drug release.

SUMMARY OF RESEARCH WORK

Herein, we report for the first time the encapsulation of hydrophilic (later functionalized with oleic acid) IONPs in PLGA using flash nanoprecipitation. Initially, flash nanoprecipitation was used to create bare PLGA nanoparticles. Paclitaxel and IONPs were then co-encapsulated in PLGA. More Fe content was observed to be encapsulated in PLGA when the concentration of IONPs in flash nanoprecipitation increased from 1 mg/ml to 3 mg/ml. However, at concentrations of 4 mg/ml to 6 mg/ml, the IONPs precipitate more quickly than PLGA and adhere to the PLGA's outside surface rather than being encapsulated. Using the magneTherm, magnetically controlled drug release was investigated.

The findings of this work indicate that flash nanoprecipitation can be used to co-encapsulate Paclitaxel and IONPs in PLGA. Furthermore, magnetically controlled drug release from these encapsulated nanoparticles is visible. One can pursue these nanoparticles for in-vitro and in-vivo studies.

CHAPTER 5: CONCLUSION AND FUTURE RECOMMENDATIONS

One can use IONPs with narrow size distributions for encapsulation.

Temperature sensitive polymers can be used for encapsulation, as they will release drug as a function of temperature as well in MagneTherm.

These PLGA encapsulated IONPs can be further pursued for in-vitro and in-vivo drug release studies.

REFERENCES

1. Solaro, R., F. Chiellini, and A. Battisti, *Targeted Delivery of Protein Drugs by Nanocarriers*. Materials (Basel). 2010 Mar 17;3(3):1928-80. doi: 10.3390/ma3031928. eCollection 2010 Mar.
2. Immordino, M.L., F. Dosio, and L. Cattel, *Stealth liposomes: review of the basic science, rationale, and clinical applications, existing and potential*. Int J Nanomedicine, 2006. **1**(3): p. 297-315.
3. Steichen, S.D., M. Caldorera-Moore, and N.A. Peppas, *A review of current nanoparticle and targeting moieties for the delivery of cancer therapeutics*. Eur J Pharm Sci, 2013. **48**(3): p. 416-27.
4. Galindo-Rodriguez, S.A., et al., *Polymeric nanoparticles for oral delivery of drugs and vaccines: a critical evaluation of in vivo studies*. Crit Rev Ther Drug Carrier Syst, 2005. **22**(5): p. 419-64.
5. Oliveira, R.R., et al., *Triggered release of paclitaxel from magnetic solid lipid nanoparticles by magnetic hyperthermia*. Mater Sci Eng C Mater Biol Appl, 2018. **92**: p. 547-553.
6. Laid, T.M., et al., *Optimizing the biosynthesis parameters of iron oxide nanoparticles using central composite design*. Journal of Molecular Structure, 2021. **1229**: p. 129497.
7. Liu, J.P., et al., *Nanoscale magnetic materials and applications*. 2009: Springer.
8. Behzadi, S., et al., *Cellular uptake of nanoparticles: journey inside the cell*. Chemical society reviews, 2017. **46**(14): p. 4218-4244.
9. Mullin, J.W., *Crystallization*. 2001: Elsevier.
10. Bandyopadhyay, S., *Fabrication and application of nanomaterials*. 2019: McGraw-Hill Education.
11. Bahrig, L., S.G. Hickey, and A. Eychmüller, *Mesocrystalline materials and the involvement of oriented attachment—a review*. CrystEngComm, 2014. **16**(40): p. 9408-9424.
12. Cao, G., *Nanostructures & nanomaterials: synthesis, properties & applications*. 2004: Imperial college press.

13. Yusefi, M., et al., *Evaluating anticancer activity of plant-mediated synthesized iron oxide nanoparticles using Punica granatum fruit peel extract*. Journal of Molecular Structure, 2020. **1204**: p. 127539.
14. Fang, S., D. Bresser, and S. Passerini, *Transition metal oxide anodes for electrochemical energy storage in lithium-and sodium-ion batteries*. Transition Metal Oxides for Electrochemical Energy Storage, 2022: p. 55-99.
15. Tuharin, K., et al., *Iron oxide and iron sulfide films prepared for dye-sensitized solar cells*. Materials, 2020. **13**(8): p. 1797.
16. Andrade, R.G., S.R. Veloso, and E.M. Castanheira, *Shape anisotropic iron oxide-based magnetic nanoparticles: Synthesis and biomedical applications*. International journal of molecular sciences, 2020. **21**(7): p. 2455.
17. Magdanz, V., et al., *Sperm-particle interactions and their prospects for charge mapping*. Advanced Biosystems, 2019. **3**(9): p. 1900061.
18. Rui, M., et al., *Iron oxide nanoparticles as a potential iron fertilizer for peanut (Arachis hypogaea)*. Frontiers in plant science, 2016. **7**: p. 815.
19. Hofmann, P., *Solid state physics: an introduction*. 2022: John Wiley & Sons.
20. Blundell, S., *Magnetism in condensed matter*. 2001: OUP Oxford.
21. Coey, J.M., *Magnetism and magnetic materials*. 2010: Cambridge university press.
22. Krishna, D.N.G., et al., *Phase identification in binary mixture of nanopowders from deconvoluted valence band spectra using X-ray photoelectron spectroscopy: Case study with iron oxide and titania polymorphs*. Applied Surface Science, 2018. **462**: p. 932-943.
23. Ansari, S.A.M.K., et al., *Magnetic iron oxide nanoparticles: synthesis, characterization and functionalization for biomedical applications in the central nervous system*. Materials, 2019. **12**(3): p. 465.
24. Shi, D., et al., *Photo-fluorescent and magnetic properties of iron oxide nanoparticles for biomedical applications*. Nanoscale, 2015. **7**(18): p. 8209-8232.
25. Lu, A.H., E.e.L. Salabas, and F. Schüth, *Magnetic nanoparticles: synthesis, protection, functionalization, and application*. Angewandte Chemie International Edition, 2007. **46**(8): p. 1222-1244.
26. Lassoued, A., et al., *Synthesis, photoluminescence and Magnetic properties of iron oxide (α -Fe₂O₃) nanoparticles through precipitation or hydrothermal methods*. Physica E: Low-dimensional Systems and Nanostructures, 2018. **101**: p. 212-219.

27. Sathya, K., R. Saravanathamizhan, and G. Baskar, *Ultrasound assisted phytosynthesis of iron oxide nanoparticle*. Ultrasonics sonochemistry, 2017. **39**: p. 446-451.
28. Velusamy, P., et al., *Synthesis of oleic acid coated iron oxide nanoparticles and its role in anti-biofilm activity against clinical isolates of bacterial pathogens*. Journal of the Taiwan Institute of Chemical Engineers, 2016. **59**: p. 450-456.
29. Golkhatmi, F.M., B. Bahramian, and M. Mamarabadi, *Application of surface modified nano ferrite nickel in catalytic reaction (epoxidation of alkenes) and investigation on its antibacterial and antifungal activities*. Materials Science and Engineering: C, 2017. **78**: p. 1-11.
30. Otsuka, H., Y. Nagasaki, and K. Kataoka, *PEGylated nanoparticles for biological and pharmaceutical applications*. Advanced drug delivery reviews, 2003. **55**(3): p. 403-419.
31. Easo, S.L. and P. Mohanan, *Dextran stabilized iron oxide nanoparticles: synthesis, characterization and in vitro studies*. Carbohydrate polymers, 2013. **92**(1): p. 726-732.
32. Roque, A.C., et al., *Biocompatible and bioactive gum Arabic coated iron oxide magnetic nanoparticles*. Journal of biotechnology, 2009. **144**(4): p. 313-320.
33. Mirabello, G., J.J. Lenders, and N.A. Sommerdijk, *Bioinspired synthesis of magnetite nanoparticles*. Chemical Society Reviews, 2016. **45**(18): p. 5085-5106.
34. Arsalani, S., et al., *Synthesis of radioluminescent iron oxide nanoparticles functionalized by anthracene for biomedical applications*. Colloids and Surfaces A: Physicochemical and Engineering Aspects, 2020. **602**: p. 125105.
35. Wu, W., et al., *Recent progress on magnetic iron oxide nanoparticles: synthesis, surface functional strategies and biomedical applications*. Science and technology of advanced materials, 2015. **16**(2): p. 023501.
36. Hui, C., et al., *Core-shell Fe₃O₄@ SiO₂ nanoparticles synthesized with well-dispersed hydrophilic Fe₃O₄ seeds*. Nanoscale, 2011. **3**(2): p. 701-705.
37. Wu, C., C. Lin, and Y. Chen, *Using glucose-bound Fe₃O₄ magnetic nanoparticles as photothermal agents for targeted hyperthermia of cancer cells*. J. Nanomed. Nanotechnol, 2015. **6**(1000264): p. 1-7.
38. Shen, L., B. Li, and Y. Qiao, *Fe₃O₄ nanoparticles in targeted drug/gene delivery systems*. Materials, 2018. **11**(2): p. 324.
39. Ali, A., et al., *Synthesis, characterization, applications, and challenges of iron oxide nanoparticles*. Nanotechnology, science and applications, 2016: p. 49-67.

40. Cardoso, V.F., et al., *Advances in magnetic nanoparticles for biomedical applications*. Advanced healthcare materials, 2018. **7**(5): p. 1700845.
41. Arias, L.S., et al., *Iron oxide nanoparticles for biomedical applications: A perspective on synthesis, drugs, antimicrobial activity, and toxicity*. Antibiotics, 2018. **7**(2): p. 46.
42. Hernández-Hernández, A.A., et al., *Iron oxide nanoparticles: synthesis, functionalization, and applications in diagnosis and treatment of cancer*. Chemical Papers, 2020. **74**(11): p. 3809-3824.
43. Ghazanfari, M.R., et al., *Perspective of Fe₃O₄ nanoparticles role in biomedical applications*. Biochemistry research international, 2016. **2016**.
44. Yew, Y.P., et al., *Green biosynthesis of superparamagnetic magnetite Fe₃O₄ nanoparticles and biomedical applications in targeted anticancer drug delivery system: A review*. Arabian Journal of Chemistry, 2020. **13**(1): p. 2287-2308.
45. Moniri, M., et al., *In vitro molecular study of wound healing using biosynthesized bacteria nanocellulose/silver nanocomposite assisted by bioinformatics databases*. International journal of nanomedicine, 2018: p. 5097-5112.
46. Zhang, S., et al., *Preparation and characterization of thermosensitive PNIPAA-coated iron oxide nanoparticles*. Nanotechnology, 2008. **19**(32): p. 325608.
47. Barrow, M., et al., *Design considerations for the synthesis of polymer coated iron oxide nanoparticles for stem cell labelling and tracking using MRI*. Chemical Society Reviews, 2015. **44**(19): p. 6733-6748.
48. Ebrahimi, M., *A short review on Ferrofluids surface modification by natural and biocompatible polymers*. Nanomedicine Journal, 2016. **3**(3): p. 155-158.
49. Avazzadeh, R., et al., *Synthesis and application of magnetite dextran-spermine nanoparticles in breast cancer hyperthermia*. Prog Biomater, 2017. **6**(3): p. 75-84.
50. Nguyen, D., *BIODEGRADABLE GELATIN DECORATED Fe₃O₄ NANOPARTICLES FOR PACLITAXEL DELIVERY*. Vietnam Journal of Science and Technology, 2018. **55**: p. 7.
51. Ghazanfari, M.R., et al., *Perspective of Fe₃O₄ Nanoparticles Role in Biomedical Applications*. Biochemistry Research International, 2016. **2016**: p. 7840161.
52. Kandasamy, G., et al., *Functionalized Hydrophilic Superparamagnetic Iron Oxide Nanoparticles for Magnetic Fluid Hyperthermia Application in Liver Cancer Treatment*. ACS Omega, 2018. **3**(4): p. 3991-4005.

53. Zhao, W., et al., *Multifunctional Fe₃O₄@WO₃@mSiO₂-APTES nanocarrier for targeted drug delivery and controllable release with microwave irradiation triggered by WO₃*. *Materials Letters*, 2016. **169**: p. 185-188.
54. Davarpanah, A., R. Shirmohammadi, and B. Mirshekari, *Experimental evaluation of polymer-enhanced foam transportation on the foam stabilization in the porous media*. *International Journal of Environmental Science and Technology*, 2019. **16**.
55. Kunieda, H. and M. Yamagata, *Mixing of nonionic surfactants at water-oil interfaces in microemulsions*. *Langmuir*, 1993. **9**(12): p. 3345-3351.
56. Ma, H.-l., et al., *Preparation and characterization of superparamagnetic iron oxide nanoparticles stabilized by alginate*. *International Journal of Pharmaceutics*, 2007. **333**(1): p. 177-186.
57. Unsoy, G., et al., *Synthesis of Doxorubicin loaded magnetic chitosan nanoparticles for pH responsive targeted drug delivery*. *European Journal of Pharmaceutical Sciences*, 2014. **62**: p. 243-250.
58. Mak, S.Y. and D.H. Chen, *Binding and sulfonation of poly (acrylic acid) on Iron oxide nanoparticles: a novel, magnetic, strong acid cation nano-adsorbent*. *Macromolecular rapid communications*, 2005. **26**(19): p. 1567-1571.
59. Gao, G.H., et al., *pH-responsive polymeric micelle based on PEG-poly(β -amino ester)/(amido amine) as intelligent vehicle for magnetic resonance imaging in detection of cerebral ischemic area*. *Journal of Controlled Release*, 2011. **155**(1): p. 11-17.
60. Li, K., et al., *Surfactant-free emulsion polymerization stabilized by ultrasmall superparamagnetic iron oxide particles using acrylic acid or methacrylic acid as auxiliary comonomers*. *Macromolecules*, 2016. **49**(20): p. 7609-7624.
61. Kurdtabar, M. and G. Rezanejade Bardajee, *Drug release and swelling behavior of magnetic iron oxide nanocomposite hydrogels based on poly (acrylic acid) grafted onto sodium alginate*. *Polymer Bulletin*, 2020. **77**(6): p. 3001-3015.
62. Nie, L., et al., *Poly (acrylic acid) capped iron oxide nanoparticles via ligand exchange with antibacterial properties for biofilm applications*. *Colloids and Surfaces B: Biointerfaces*, 2021. **197**: p. 111385.
63. Benassai, E., et al., *High-throughput large scale microfluidic assembly of iron oxide nanoflowers@ PS-b-PAA polymeric micelles as multimodal nanoplatfoms for photothermia and magnetic imaging*. *Nanoscale Advances*, 2024. **6**(1): p. 126-135.
64. Bugno, J., H.J. Hsu, and S. Hong, *Tweaking dendrimers and dendritic nanoparticles for controlled nano-bio interactions: potential nanocarriers for improved cancer targeting*. *J Drug Target*, 2015. **23**(7-8): p. 642-50.

65. Mitchell, M.J., et al., *Engineering precision nanoparticles for drug delivery*. Nature Reviews Drug Discovery, 2021. **20**(2): p. 101-124.
66. Kammari, R., N. Das, and S. Das, *Nanoparticulate Systems for Therapeutic and Diagnostic Applications*. 2017. p. 105-144.
67. Hernández-Giottonini, K.Y., et al., *PLGA nanoparticle preparations by emulsification and nanoprecipitation techniques: effects of formulation parameters*. RSC Adv, 2020. **10**(8): p. 4218-4231.
68. Johnson, B. and R. Prud'homme, *Flash NanoPrecipitation of Organic Actives and Block Copolymers using a Confined Impinging Jets Mixer*. Australian Journal of Chemistry - AUST J CHEM, 2003. **56**.
69. Liu, Y., et al., *Mixing in a multi-inlet vortex mixer (MIVM) for flash nano-precipitation*. Chemical Engineering Science, 2008. **63**(11): p. 2829-2842.
70. Caggiano, N.J., et al., *Sequential Flash NanoPrecipitation for the scalable formulation of stable core-shell nanoparticles with core loadings up to 90%*. International Journal of Pharmaceutics, 2023. **640**: p. 122985.
71. Liu, Y., et al., *Formulation of Nanoparticles Using Mixing-Induced Nanoprecipitation for Drug Delivery*. Industrial & Engineering Chemistry Research, 2019. **XXXX**.
72. Tao, J., S.F. Chow, and Y. Zheng, *Application of flash nanoprecipitation to fabricate poorly water-soluble drug nanoparticles*. Acta Pharmaceutica Sinica B, 2019. **9**(1): p. 4-18.
73. Han, J., et al., *Polymer-Based Nanomaterials and Applications for Vaccines and Drugs*. Polymers (Basel), 2018. **10**(1).
74. Pustulka, K.M., et al., *Flash nanoprecipitation: particle structure and stability*. Molecular pharmaceutics, 2013. **10**(11): p. 4367-4377.
75. Zhu, Z., *Effects of amphiphilic diblock copolymer on drug nanoparticle formation and stability*. Biomaterials, 2013. **34**(38): p. 10238-10248.
76. Pinkerton, N.M., et al., *Single-Step Assembly of Multimodal Imaging Nanocarriers: MRI and Long-Wavelength Fluorescence Imaging*. Advanced Healthcare Materials, 2015. **4**(9): p. 1376-1385.
77. Shen, H., et al., *Self-assembling process of flash nanoprecipitation in a multi-inlet vortex mixer to produce drug-loaded polymeric nanoparticles*. Journal of Nanoparticle Research, 2011. **13**: p. 4109-4120.

78. Reisch, A., et al., *Tailoring fluorescence brightness and switching of nanoparticles through dye organization in the polymer matrix*. ACS applied materials & interfaces, 2017. **9**(49): p. 43030-43042.
79. Zhao, L.-Y., et al., *Magnetic-mediated hyperthermia for cancer treatment: Research progress and clinical trials*. Chinese Physics B, 2013. **22**(10): p. 108104.
80. Latorre, M. and C. Rinaldi, *Applications of magnetic nanoparticles in medicine: magnetic fluid hyperthermia*. Puerto Rico health sciences journal, 2009. **28**(3).
81. Maity, D., et al., *Novel synthesis of superparamagnetic magnetite nanoclusters for biomedical applications*. Journal of Materials Chemistry, 2011. **21**(38): p. 14717-14724.
82. Mangaiyarkarasi, R., et al., *Paclitaxel conjugated Fe₃O₄@LaF₃:Ce³⁺, Tb³⁺ nanoparticles as bifunctional targeting carriers for Cancer theranostics application*. Journal of Magnetism and Magnetic Materials, 2016. **399**: p. 207-215.
83. Al-Amiery, A.A., et al., *Synthesis and characterization of a novel eco-friendly corrosion inhibition for mild steel in 1 M hydrochloric acid*. Scientific Reports, 2016. **6**(1): p. 19890.
84. Menon, J.U., et al., *Dual-Drug Containing Core-Shell Nanoparticles for Lung Cancer Therapy*. Scientific Reports, 2017. **7**(1): p. 13249.
85. Dou, W., et al., *Investigation of GeSn Strain Relaxation and Spontaneous Composition Gradient for Low-Defect and High-Sn Alloy Growth*. Scientific Reports, 2018. **8**(1): p. 5640.
86. Albukhaty, S., et al., *Investigation of Dextran-Coated Superparamagnetic Nanoparticles for Targeted Vinblastine Controlled Release, Delivery, Apoptosis Induction, and Gene Expression in Pancreatic Cancer Cells*. Molecules, 2020. **25**: p. 4721.
87. Abdul Mahdi, S., et al., *Gene expression and apoptosis response in hepatocellular carcinoma cells induced by biocompatible polymer/magnetic nanoparticles containing 5-fluorouracil*. Electronic Journal of Biotechnology, 2021. **52**: p. 21-29.
88. Al-Kinany, M., A. Haider, and S. Al-Musawi, *Design and Synthesis of Nanoencapsulation with a New Formulation of Fe@Au-CS-CU-FA NPs by Pulsed Laser Ablation in Liquid (PLAL) Method in Breast Cancer Therapy: In Vitro and In Vivo*. Plasmonics, 2021. **16**.
90. Al-Musawi, S., et al., *Design and Synthesis of Multi-Functional Superparamagnetic Core-Gold Shell Nanoparticles Coated with Chitosan and Folate for Targeted Antitumor Therapy*. Nanomaterials, 2020. **11**: p. 32.

91. Haider, A., et al., *Formulation of Curcumin in Folate Functionalized Polymeric Coated Fe₃O₄@Au Core-Shell Nanosystem for Targeting Breast Cancer Therapy*. 2022.
92. Al-Saedi, S., et al., *Improvement of Li-ion batteries energy storage by graphene additive*. Energy Reports, 2019. **6**.
93. Rashid, M., et al., *Vancomycin conjugated iron oxide nanoparticles for magnetic targeting and efficient capture of Gram-positive and Gram-negative bacteria*. RSC advances, 2021. **11**(57): p. 36319-36328.
94. Ali, Z., J.-P. Andreassen, and S. Bandyopadhyay, *Fine-tuning of particle size and morphology of silica coated iron oxide nanoparticles*. Industrial & Engineering Chemistry Research, 2023. **62**(12): p. 4831-4839.
95. Saad, W.S. and R.K. Prud'homme, *Principles of nanoparticle formation by flash nanoprecipitation*. Nano Today, 2016. **11**(2): p. 212-227.
96. Lai, C.W., et al., *Iron oxide nanoparticles decorated oleic acid for high colloidal stability*. Advances in Polymer Technology, 2018. **37**(6): p. 1712-1721.
97. Nadeem, M., et al., *Synthesis and Characterisation of Oleic Acid Coated Fe₃O₄ Nanoparticles in Poly Alpha Olefin Oil based Nanofluid for Heat Transfer Applications*. International Journal of Nanoelectronics and Materials (IJNeM), 2021. **14**(1): p. 37-48.
98. Anbarasu, M., et al., *Synthesis and characterization of polyethylene glycol (PEG) coated Fe₃O₄ nanoparticles by chemical co-precipitation method for biomedical applications*. Spectrochimica Acta Part A: Molecular and Biomolecular Spectroscopy, 2015. **135**: p. 536-539.
99. Qu, J., et al., *Preparation of Fe₃O₄-chitosan nanoparticles used for hyperthermia*. Advanced Powder Technology, 2010. **21**(4): p. 461-467.
100. Jiang, C., et al., *Magnetically assembled iron oxide nanoparticle coatings and their integration with pseudo-spin-valve thin films*. Journal of Materials Chemistry C, 2017. **5**(2): p. 252-263.
101. Shi, Y.-y., et al., *Size-controlled and large-scale synthesis of organic-soluble Ag nanocrystals in water and their formation mechanism*. Progress in Natural Science: Materials International, 2011. **21**(6): p. 447-454.
102. Yang, K., et al., *Re-examination of characteristic FTIR spectrum of secondary layer in bilayer oleic acid-coated Fe₃O₄ nanoparticles*. Applied Surface Science, 2010. **256**(10): p. 3093-3097.

103. De Roo, J., et al., *Unravelling the Surface Chemistry of Metal Oxide Nanocrystals, the Role of Acids and Bases*. Journal of the American Chemical Society, 2014. **136**(27): p. 9650-9657.
104. Feczkó, T., et al., *Influence of process conditions on the mean size of PLGA nanoparticles*. Chemical Engineering and Processing: Process Intensification, 2011. **50**(8): p. 846-853.
105. Johnson, B.K. and R.K. Prud'homme, *Flash nanoprecipitation of organic actives and block copolymers using a confined impinging jets mixer*. Australian Journal of Chemistry, 2003. **56**(10): p. 1021-1024.
106. Atkinson, W.J., I.A. Brezovich, and D.P. Chakraborty, *Usable frequencies in hyperthermia with thermal seeds*. IEEE Transactions on Biomedical Engineering, 1984(1): p. 70-75.
107. Wang, Y., et al., *Nanopore generation in biodegradable silk/magnetic nanoparticle membranes by an external magnetic field for implantable drug delivery*. ACS Applied Materials & Interfaces, 2022. **14**(35): p. 40418-40426.
108. Narayanaswamy, V., et al., *Role of magnetite nanoparticles size and concentration on hyperthermia under various field frequencies and strengths*. Molecules, 2021. **26**(4): p. 796.